

## Methods for Dynamic Contrast Enhanced MRI

van Schie, Jeroen

**DOI**

[10.4233/uuid:31e9f07b-4070-4a53-8c82-57c26a2bcae6](https://doi.org/10.4233/uuid:31e9f07b-4070-4a53-8c82-57c26a2bcae6)

**Publication date**

2016

**Document Version**

Final published version

**Citation (APA)**

van Schie, J. (2016). *Methods for Dynamic Contrast Enhanced MRI*. [Dissertation (TU Delft), Delft University of Technology]. <https://doi.org/10.4233/uuid:31e9f07b-4070-4a53-8c82-57c26a2bcae6>

**Important note**

To cite this publication, please use the final published version (if applicable).  
Please check the document version above.

**Copyright**

Other than for strictly personal use, it is not permitted to download, forward or distribute the text or part of it, without the consent of the author(s) and/or copyright holder(s), unless the work is under an open content license such as Creative Commons.

**Takedown policy**

Please contact us and provide details if you believe this document breaches copyrights.  
We will remove access to the work immediately and investigate your claim.

# Methods for Dynamic Contrast Enhanced MRI



# Methods for Dynamic Contrast Enhanced MRI

Proefschrift

ter verkrijging van de graad van doctor  
aan de Technische Universiteit Delft,  
op gezag van de Rector Magnificus prof.ir. K.C.A.M. Luyben;  
voorzitter van het College voor Promoties,  
in het openbaar te verdedigen op woensdag 21 december 2016 om 12:30 uur

door

Jeroen Johannes Nicolaas van SCHIE

natuurkundig ingenieur  
geboren te Naaldwijk, Nederland

Dit proefschrift is goedgekeurd door de  
promotoren: Prof. dr. ir. L.J. van Vliet  
Prof. dr. J. Stoker  
copromotoren: Dr. F. M. Vos  
Dr. C. Lavini

Samenstelling promotiecommissie:

Rector Magnificus,	Voorzitter
Prof. dr. ir. L.J. van Vliet,	Technische Universiteit Delft, promotor
Prof. dr. J. Stoker,	Academisch Medisch Centrum, promotor
Dr. F. M. Vos,	Technische Universiteit Delft, copromotor
Dr. C. Lavini,	Academisch Medisch Centrum, copromotor

*Onafhankelijke leden:*

Prof.dr. W.J. Niessen,	Technische Universiteit Delft
Prof.dr.ir. G.J. Strijkers,	Academisch Medisch Centrum, Amsterdam
Prof.dr. U.A. van der Heide,	Nederlands Kanker Instituut, Amsterdam Leids Universitair Medisch Centrum, Leiden
Dr. D.H.J. Poot,	Erasmus Medisch Centrum, Rotterdam
Prof.dr. A.M. Vossepoel,	Technische Universiteit Delft, reservelid



The work in this thesis was conducted at the Quantitative Imaging Group (QI), Faculty of Applied Sciences, Delft University of Technology.

The work was financially supported by VIGOR++ (European Union's Seventh Framework Program, No. 270379).

Cover design: proefschriftmaken.nl, Vianen

Printed by: proefschriftmaken.nl, Vianen

Published by: Uitgeverij BOXPress, Vianen

ISBN: 978-94-6295-521-9

Copyright © 2016 by J.J.N. van Schie

A digital copy can be downloaded from [repository.tudelft.nl](http://repository.tudelft.nl).

# Contents

---

1	Introduction .....	1
1.1	Magnetic Resonance Imaging .....	2
1.2	Dynamic Contrast Enhanced MRI .....	2
1.3	Challenges.....	3
1.4	Thesis Outline .....	5
1.5	References .....	6
2	Principles of Dynamic Contrast Enhanced MRI.....	7
2.1	Magnetic Resonance .....	8
2.1.1	Spin Dynamics .....	8
2.1.2	Relaxation.....	9
2.2	The MRI Scanner – Coils .....	10
2.3	Magnetic Resonance Imaging .....	12
2.3.1	Gradient Echo .....	12
2.3.2	Spatial Encoding .....	12
2.4	Common Sequences.....	14
2.4.1	Fast Spoiled Gradient Echo .....	14
2.4.2	Inversion Recovery .....	15
2.5	Contrast Agents .....	16
2.6	DCE-MRI and Pharmacokinetic Modelling .....	17
2.6.1	Tofts’ Model.....	18
2.7	References .....	20
3	Feasibility of a Fast Method for $B_1$ -Inhomogeneity Correction for FSPGR Sequences .....	21
3.1	Introduction .....	22

3.1.1	Related Work .....	22
3.1.2	Objective .....	24
3.2	Methods.....	24
3.2.1	Experimental Material .....	24
3.2.2	Look-Locker $T_1$ -map .....	25
3.2.3	Variable Flip Angle $T_1$ -map.....	26
3.2.4	$B_1$ -inhomogeneity map and VFA $T_1$ -map.....	27
3.2.5	Inversion Recovery, reference $T_1$ -mapping .....	28
3.2.6	Statistical Analysis.....	29
3.3	Results .....	29
3.3.1	In vitro $T_1$ -maps .....	29
3.3.2	In vitro $B_1$ -inhomogeneity maps.....	31
3.3.3	In vivo $T_1$ -maps.....	32
3.3.4	In vivo $B_1$ -inhomogeneity maps.....	35
3.4	Discussion.....	36
3.4.1	In vitro experiments.....	36
3.4.2	In vivo experiments .....	37
3.4.3	Limitations .....	38
3.5	Conclusion.....	39
3.6	Acknowledgements .....	39
3.7	References .....	39
4	Estimating the AIF from DCE-MRI Data with Compensation for Flow Enhancement (I): Theory, Method and Phantom Experiments.....	43
4.1	Introduction .....	44
4.1.1	Related Work .....	44
4.1.2	Objective .....	45

4.2	Materials and Methods .....	46
4.2.1	Theory.....	46
4.2.2	Simulation.....	52
4.2.3	Phantom experiment .....	53
4.3	Results .....	56
4.3.1	Simulation Results.....	56
4.3.2	Phantom Experiment Results .....	58
4.4	Discussion.....	60
4.4.1	Simulation.....	60
4.4.2	Phantom Experiments .....	61
4.4.3	Limitations .....	61
4.5	Conclusion.....	62
4.6	Acknowledgements .....	62
4.7	Appendix .....	62
4.7.1	Appendix A: Derivation of the Formula for $M_z$ in Explicit Form ...	62
4.8	References .....	63
5	Estimating the AIF from DCE-MRI Data with Compensation for Flow Enhancement (II): Applications in Spine Diagnostics and Assessment of Crohn's Disease.....	67
5.1	Introduction .....	68
5.2	Materials and Methods .....	69
5.2.1	Theory.....	69
5.2.2	Patients.....	70
5.2.3	MRI Acquisition Protocols.....	71
5.2.4	Artery Selection and AIF Estimation .....	71
5.2.5	Pharmacokinetic Analysis .....	73
5.3	Results .....	74



5.3.1	Results from the Spine Data .....	74
5.3.2	Results from the Crohn's Disease data.....	77
5.4	Discussion.....	80
5.4.1	The Spine Data .....	80
5.4.2	The Crohn's Disease Data.....	81
5.4.3	AIF Tail Offset.....	81
5.4.4	Limitations.....	82
5.5	Conclusion.....	83
5.6	Acknowledgements .....	83
5.7	Appendix .....	84
5.7.1	Aorta segmentation from the Crohn's Disease data .....	84
5.8	References .....	85
6	Conclusion .....	89
6.1	Simultaneous $T_1$ - and $B_1$ -mapping.....	90
6.2	Estimating the AIF with Compensation for Flow Enhancement.....	91
6.3	Future Work.....	92
	Summary.....	93
	Samenvatting.....	95
	Acknowledgements.....	97
	Curriculum Vitae.....	98

# 1 Introduction

---

## **1.1 Magnetic Resonance Imaging**

Magnetic Resonance Imaging (MRI) is one of the most widely used imaging techniques in modern medicine. It is used to visualise the internal structures of patients and the functioning of organs in a three-dimensional, non-invasive manner. The contrast generating mechanism in MRI can be chosen from an extensive suite of imaging sequences, which results in images with a large variety of contrast in soft tissues. Nowadays, the MRI images are irreplaceable radiological tools for the detection of lesions, diagnosis, the assessment of the current status of diseases, monitoring the effect of medication and the planning of surgery. MRI operates without any harmful ionizing radiation, and can be used repeatedly for imaging any body part, in any desired direction.

## **1.2 Dynamic Contrast Enhanced MRI**

Over the past decades, Dynamic Contrast Enhanced MRI (DCE-MRI) was developed for imaging tissues during an intravenous injection of a contrast agent (typically gadolinium-based). Here, the time-dependent change in the measured signal intensity effected by the contrast agent is used as an indicator for tissue integrity.

With the advent of new, fast imaging techniques, the reduction in acquisition time of MRI images has allowed the acquisition of DCE-MRI with a time resolution in the order of seconds. With this technique, the response of tissues to the injection of a contrast-enhancing agent into the patient's blood stream is monitored over time. The behaviour of the contrast agent in the tissues can then be then modelled by a pharmacokinetic model.

Pharmacokinetic models describe how the concentration of contrast agent in a tissue changes in response to the presence of contrast agent in the blood, according to the local tissue properties. The pharmacokinetic model parameters therefore reflect the physiological properties of the tissue. In some pathologies, these physiological properties are different from the healthy case, and are therefore used

to visualize characteristics of the pathology. For example, diseases such as cancer or inflammatory diseases may increase the microvascular permeability of capillaries, a property that can be measured by some models.

To be able to meaningfully compare the results of multiple pharmacokinetic analyses, the results of the analyses must be quantitative, accurate and precise. For this, the pharmacokinetic model requires knowledge of the actual concentrations of contrast agent in both the tissue of interest and in the blood plasma. This thesis aims to provide methods to accurately measure these quantities.

### **1.3 Challenges**

A range of quantitative pharmacokinetic models exists for the analysis of DCE-MRI data, ranging from generally applicable models to models for specific organs and specific contrast agents. The most reliable models require knowledge of the concentrations of contrast agent in the tissue of interest as input.

However, in MRI, the relation between the concentration of contrast agent and the signal intensity is not straightforward, as the MRI signal is not generated by the contrast agent itself (contrary to other imaging modalities such as PET or CT). In MRI, the signal is generated by the nuclear spins of hydrogen atoms, which change their intrinsic properties in the presence of a paramagnetic contrast agent. More specifically, the tissue's spin-lattice relaxation time  $T_1$  and the spin-spin relaxation times  $T_2$  and  $T_2^*$  are affected by the contrast agent. Knowledge of these relaxation times is essential for converting the MRI signal into the desired measure of contrast agent concentration.

The conversion of signal to concentration is further hindered by the fact that the local  $B_1$  field (i.e., the magnetic component of the electromagnetic waves used to excite the spins) may be inhomogeneous. This results in inaccurate estimates of the intensity of the applied RF-pulse. The estimation of a reliable  $T_1$ -map and  $B_1$ -map is therefore a necessary step to correctly convert the measured MRI signals to concentration. Additionally, patient motion, such as breathing, is a significant problem when imaging the abdominal area, as it introduces imaging artifacts. This

means that the  $T_1$ - or  $B_1$ -maps must be obtained within breath-holds, posing an additional challenge.

Many pharmacokinetic models use as input the contrast agent concentration in the blood of a feeding artery to the tissue of interest. This is often referred to as the arterial input function (AIF). Again, the MRI signal intensity depends on the concentration of contrast agent in the blood, the  $T_1$  of the blood, the sequence parameters, and, through the applied RF-pulse, also by the local  $B_1$  inhomogeneity. However, an additional complication of measuring the AIF is caused by the blood flow during the MRI scan. Blood that has just entered the field of view produces an increased signal intensity compared to blood which has already spent some time inside the field of view. More precisely, the MRI signal intensity depends on the number of radiofrequency pulses that the spins have received. The contrast agent concentration is computed from the ratio of the post-contrast signal and the pre-contrast signal, and an enhancement of both these signals leads to a lower ratio. The inflow effect therefore causes an underestimation of the contrast agent concentration, if it is not accounted for. Additionally, the ambiguity between signal enhancement due to the inflow effect and signal enhancement due to the presence of contrast agent makes that neither the number of pulses nor the concentration can be computed directly.

The research presented in this thesis was initiated by the VIGOR++ project. This project focused on the research and development of ICT tools for the analysis, modelling and simulation of human physiology and disease processes of the gastrointestinal tract (1). One objective was to create patient-specific instruments to quantitatively assess the status of Crohn's Disease. The work presented in this thesis contributes to the VIGOR++ project by providing novel methods for the measurement of pharmacokinetic parameters of diseased bowel tissues using DCE-MRI. These pharmacokinetic measurements can then be used in conjunction with other measurements, such as the bowel wall thickness, to predict the severity of Crohn's Disease.

The work presented in this thesis can be summarized in the following objectives:

**Objective 1:** We aim to estimate a reliable  $T_1$  map in the presence of  $B_1$  inhomogeneities with scan sequences that can be acquired within breath-holds.

**Objective 2:** We aim to develop a method that estimates the arterial input function from DCE-MRI data, while correcting for the inflow effect.

**Objective 3:** We aim to test the effectiveness of the above method in-vivo. We test the method in large arteries where the inflow effect poses a significant problem, and provide an automated version which uses the corrected AIF in pharmacokinetic modelling.

## 1.4 Thesis Outline

**Chapter 2** provides an overview of the principles of MRI and Dynamic Contrast Enhanced MRI. Essential background information, which is necessary to understand the following chapters, is consolidated in this chapter. It describes the physical principles of MRI, and then expands to the theory of DCE-MRI. Furthermore, an introduction to pharmacokinetic modelling is given.

**Chapter 3** focuses on the measurement of a  $T_1$ -map in the presence of  $B_1$ -inhomogeneities. In order to correct for the  $B_1$ -inhomogeneities, we use two separate MRI scans, which were required to be performed within periods of breath-hold. One scan provided an accurate, but very noisy  $T_1$  map, while the other provided a biased  $T_1$ -map due to the inhomogeneous  $B_1$ -field. We present a method to combine these two scans to estimate the  $B_1$ -inhomogeneities, which we then use to compute an accurate and precise  $T_1$ -map.

**Chapter 4** focuses on the measurement of the contrast agent concentration in circulating arterial blood, taking the effects of blood flow on the MRI signal into account. We derive a theoretical relationship between the MRI signal intensity and the contrast agent concentration, which takes into account the number of pulses experienced by the spins during an MRI scan. We compare this theory to the outcome of a controlled flow phantom experiment, to verify the accuracy of our approach. Furthermore, we present a method that resolves the degeneracy between

concentration and number of pulses by forcing the resulting AIF to carry some specific characteristics of a population averaged AIF. We then verify this method by means of Monte Carlo simulations.

**Chapter 5** presents the application of the theory of Chapter 4 in-vivo, by applying the methods to two sets of patient data. In this work, we also present an automatic segmentation of the aorta. We then apply the proposed method to each segmented voxel separately, and combine the data from all voxels to create one AIF. We then use this AIF in a pharmacokinetic model. The first dataset was obtained with a variety of scan settings, which we use to assess the robustness of the method. With the second dataset, comprised of Crohn's Disease patients (from the VIGOR++ project), we correlate the obtained pharmacokinetic parameters to the clinically relevant CDEIS score.

Finally, **Chapter 6** discusses and summarizes the benefits and limitations of the presented work, and looks ahead to further challenges.

## 1.5 References

1. VIGOR++. Virtual Gastrointestinal Tract: Facts & Objectives, <http://vigorpp.eu/facts.php>, accessed 26 Aug 2016.

# 2 Principles of Dynamic Contrast Enhanced MRI

---



In this chapter, a brief overview of the principles behind MRI and Dynamic Contrast Enhanced MRI (DCE-MRI) is presented. The information in this chapter provides some essential background knowledge about the subjects covered in this thesis. Additional information can be found in (1).

## 2.1 Magnetic Resonance

### 2.1.1 Spin Dynamics

The principle of MRI relies on the fact that the nuclear net spin magnetic moment of some atoms can generate a measurable signal under specific conditions. In most cases, hydrogen nuclei ( $^1\text{H}$ ) are chosen, since hydrogen is abundantly present in the human body, in the form of water. When placed into a strong external magnetic field, the spin magnetic moments of the hydrogen nuclei (commonly referred to as ‘spins’) tend to align along this magnetic field. On a microscopic scale, thermal fluctuations cause the individual spins to be randomly distributed, with a slightly larger chance to point along the magnetic field. On a macroscopic scale, we can say that the material will have a net magnetization with an equilibrium position pointing along the magnetic field. The macroscopic magnetization  $M$  is related to the microscopic spins via Curie’s law:

$$M = \frac{C \cdot B}{T}, \quad (2.1)$$

where  $B$  is the strength of the external magnetic field,  $T$  the temperature of the material, and  $C$  the material-dependent Curie constant, which is proportional to the density of spins.

Spins in an external magnetic field experience a torque that causes them to precess around the magnetic field: the so-called Larmor precession. The Larmor precession frequency  $\omega$  is determined by the strength of the external magnetic field  $B$  and the particle-specific gyromagnetic ratio  $\gamma$ :

$$\omega = \gamma B, \quad (2.2)$$

which, for nuclear spins, lies in the radiofrequency (RF) range. When spins in a magnetic field are subjected to an oscillating electromagnetic field of the same frequency as their Larmor frequency, these spins will resonate. On a macroscopic scale, the magnetization vector will tip over by a certain flip angle  $\alpha$ , where the time-integral of the amplitude of the RF-pulse determines the size of the flip angle.

The transverse component of the precessing spins generate an oscillating electromagnetic field, which, according to Faraday's law of induction, can induce an electromotive force in a receive coil placed a small distance away. Before the application of the RF-pulse, the transverse component of the spins have an arbitrary phase, the transverse component of the net magnetization is zero, and no signal is detected. After the application of RF-pulse, the net transverse magnetization becomes nonzero, and a signal can be detected.

### 2.1.2 Relaxation

After spins have been excited by an RF-pulse, they will gradually relax back to their equilibrium state. This happens through three independent mechanisms simultaneously. First, energy is exchanged between the hydrogen nuclei and their surroundings (a process called spin-lattice interaction). On a macroscopic scale, this causes the longitudinal component of the net magnetization  $M_z$  to recover to equilibrium in an exponential fashion. The relaxation time associated with this recovery is called the  $T_1$ -time. That is:

$$M_z(t) = M_0 \cos(\alpha) \exp(-t/T_1) + M_0 (1 - \exp(-t/T_1)). \quad (2.3)$$

The typical  $T_1$ -time for hydrogen lies in the order of a second.

Second, the spins also exchange energy among each other (a process called spin-spin interaction). This causes the relative phase of individual nearby spins to disperse, which results in the transverse component of the net magnetization  $M_{xy}$  decaying to zero. This is again an exponential process, characterized by the  $T_2$ -relaxation time

Third, spins may experience static fluctuations in magnetic field strength, due to global variation in the  $B_0$  field, or susceptibility effects. As a consequence, these spins will precess with a slightly varying frequency. Similar to the spin-spin

interaction, this causes the individual spins to dephase, again resulting in an exponential decay of the transverse magnetization. This is characterized by the relaxation time  $T_2'$ . Since the  $T_2$  and  $T_2'$  effects both affect the transverse magnetization, they are often combined into one value known as  $T_2^*$ :

$$M_{xy}(t) = M_0 \sin(\alpha) \exp(-t/T_2) \exp(-t/T_2') = M_0 \sin(\alpha) \exp(-t/T_2^*), \quad (2.4)$$

with  $1/T_2^* = 1/T_2 + 1/T_2'$ . The typical  $T_2^*$ -time lies in the order of several tens of milliseconds.

## 2.2 The MRI Scanner – Coils

A modern, clinical MRI scanner is a large cylindrical device with a hole through the centre, in which patients can be positioned through a movable table. A photograph of an MRI scanner is shown in Figure 2.1.



Figure 2.1: MRI Scanner.

Source: <http://www.usa.philips.com/healthcare/product/HC781342/ingenia-30t-mr-system>

Inside the toroidal casing, several coils are housed. Particularly, a large, superconducting coil surrounds the bore, and is used to generate a strong magnetic field (typically several Tesla) inside the bore. The superconducting state is maintained by embedding the coil in liquid helium (4 Kelvin), which is shielded from the outside by layers of vacuum. The magnetic field generated by this coil is called the  $B_0$ -field, and is used to magnetize the subject in the bore.

Inside the superconducting electromagnet, several smaller coils are placed, which are used to generate gradients in the  $B_0$ -field (typically several mT/m). More specifically, the gradient coils cause the magnitude of the  $B_0$ -field to increase linearly over distance, while keeping the direction mostly<sup>1</sup> unchanged. Three sets of gradient coils are used to facilitate magnetic field gradients in each of the principal directions:  $G_x$ ,  $G_y$  and  $G_z$ .

Finally, so-called transmit and receive coils are placed inside the bore, inside the table, and also mounted in specialized, modular devices designed to fit on or around a specific body part. These coils can be used to transmit and/or receive electromagnetic waves in the radiofrequency range. The transmit coils are used to excite the spins, while the receive coils detect electromagnetic waves emitted by the excited spins. The alternating magnetic field generated by the transmit coil is called the  $B_1$ -field. A schematic overview of the coils in an MRI machine is shown in Figure 2.2.

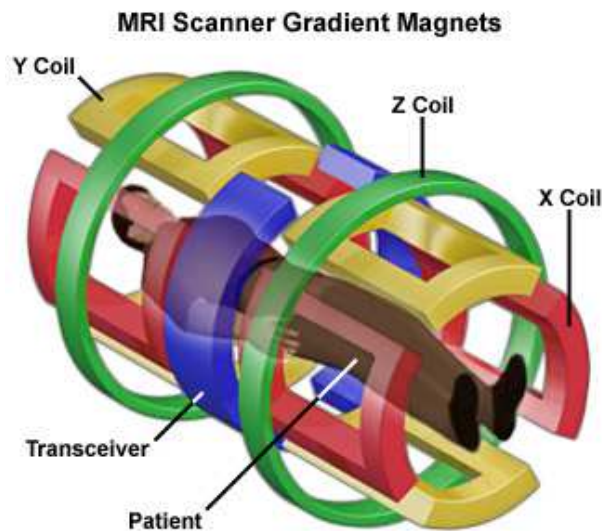


Figure 2.2: Coils inside an MRI machine.

Source: <https://nationalmaglab.org/education/magnet-academy/learn-the-basics/stories/mri-a-guided-tour>

---

<sup>1</sup> Gradient coils always introduce a small magnetic field perpendicular to the main magnetic field, to satisfy Maxwell's equations.

## 2.3 Magnetic Resonance Imaging

### 2.3.1 Gradient Echo

After the spins have been excited by an RF-pulse, their oscillating EM field is not measured immediately. Instead, a typical method of measuring the spins' signal is by causing them to 'echo'. This can be done by applying a gradient field for a short period of time, followed by a gradient field in the opposite direction for twice the amount of time<sup>2</sup>. The first part of this sequence causes the spins to dephase rapidly, while the second part causes a rephasing followed again by dephasing. When the spins have rephased, the signal once again reaches a maximum, which is called an echo. The time at which the echo occurs is called the Echo Time,  $T_E$ . Aside from generating an echo, the gradients also provide spatial encoding, which is described in the next section. See Figure 2.3 for a schematic overview of the gradient echo sequence.

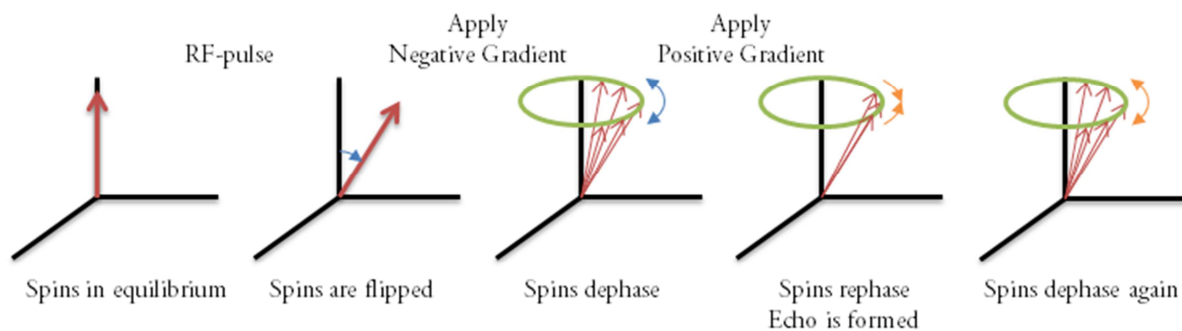


Figure 2.3: Spin dynamics during a gradient echo sequence.

### 2.3.2 Spatial Encoding

At the echo time, all excited spins generate an echo at the same frequency, and are therefore indistinguishable. Hence, a mechanism is needed to determine where each signal comes from, i.e., to generate an image through spatial encoding.

<sup>2</sup> The duration may be reduced by increasing the gradient field strength, as long as the time-integral of the gradient field strength of the second part is twice that of the first part.

There are two main methods for MR imaging: 2D and 3D imaging. In 2D imaging, a volume is imaged slice by slice, by exciting only the spins in a single slice at a time. This is done by applying a gradient field while applying a band-limited RF-pulse of a certain bandwidth. The gradient field causes the Larmor frequency to vary spatially, and only the spins with a Larmor frequency inside the bandwidth of the RF-pulse will resonate. Alternatively, in 3D imaging, the entire volume is excited simultaneously.

Inside the 2D slices, or inside the 3D slab, spatial dependency is introduced via frequency and phase encoding. For the frequency encoding, a gradient in magnetic field strength is imposed in one direction during the echo, making spins at different locations precess at different Larmor frequencies. Applying a Fourier transform to the measured signal reveals the frequency components of the signal, and therefore indirectly where each signal came from in this one direction.

For phase encoding, one (for 2D imaging) or two (for 3D imaging) additional gradients are applied for a short period of time before the echo, perpendicular to the frequency encoding direction. This causes the spins to accumulate a location dependent phase. Measuring echoes for different phase encoding gradient amplitudes, combined with the frequency encoding described above, provides a two- or three-dimensional image of the subject. The time it takes to execute one repetition of the sequence is called the Repetition Time, or  $T_R$ . See Figure 2.4 for a schematic overview of the 2D gradient echo sequence with spatial encoding.

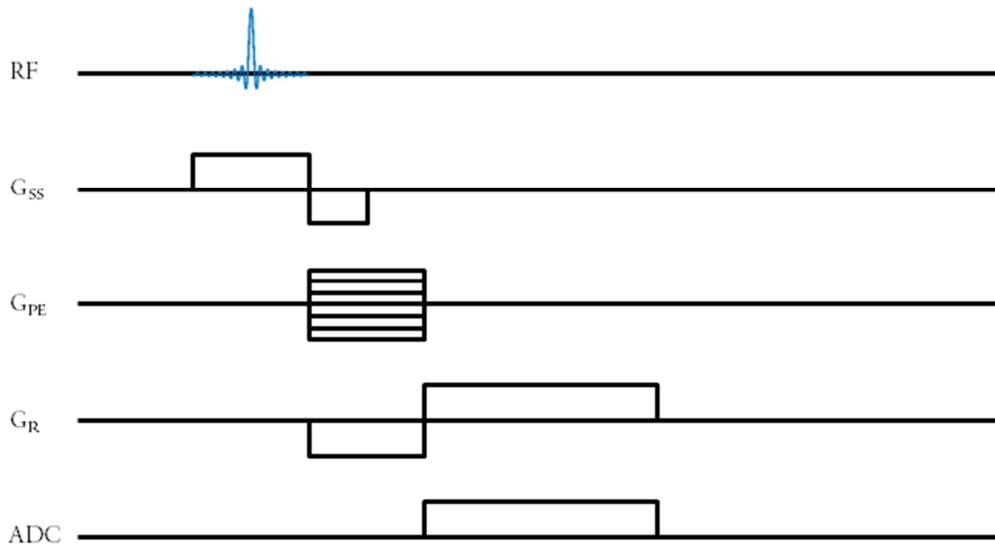


Figure 2.4: 2D gradient echo sequence diagram. From top to bottom: the RF-pulse emitted by the transmit coil, the slice select gradient, the phase encoding gradient, the read gradient, and the analogue/digital converter of the receive coil, as a function of time. The sequence is repeated for different phase encoding gradient strengths. For the 3D gradient echo sequence, the slice select gradient is not used, and a second phase encoding gradient is used instead.

## 2.4 Common Sequences

In MRI, the timing and order of applying RF-pulses, applying gradient fields, and reading the MR signal, is called a sequence. The gradient echo sequence (described in the previous section) is one of the most basic sequences, and can provide images whose contrast depends on the local Proton Density (PD),  $T_1$  and  $T_2^*$ . The amount of  $T_1$  and  $T_2^*$  weighting can be chosen by simply tuning the repetition time and echo time of the sequence, respectively. While the gradient echo sequence is already quite versatile, more advanced sequences exist. In this section, two important sequences are addressed, which will also be used further in the thesis.

### 2.4.1 Fast Spoiled Gradient Echo

The Fast Spoiled Gradient Echo (FSPGR) sequence is a sequence that produces  $T_1$  weighted images. The FSPGR sequence is a gradient echo sequence with very short  $T_R$  and  $T_E$  (in the order of several ms). However, before each RF-pulse, any transverse magnetization remaining from the previous repetition is removed, or ‘spoiled’. This is done by either applying a gradient, which dephases the spins, or by

applying each successive RF-pulse in a randomized direction, which prevents build-up of transverse magnetization.

After a number of repetitions, the recovery of the longitudinal magnetization via the  $T_1$  relaxation process is exactly countered by the reduction of the longitudinal component caused by the application of the RF-pulse<sup>3</sup>. This is called the steady state case, during which the signal generated by the spins is given by:

$$S = N \sin(\alpha) \frac{1 - \exp(-T_R / T_1)}{1 - \cos(\alpha) \exp(-T_R / T_1)} \exp(-T_E / T_2^*) \quad (2.5)$$

This sequence has a very short repetition time, and therefore facilitates a high temporal resolution. For this reason, and for its  $T_1$ -weighting, the FSPGR sequence is commonly used for Dynamic Contrast Enhanced MRI.

Another common application of the FSPGR sequence is  $T_1$ -mapping (i.e., to estimate the  $T_1$ -value of a tissue). Normally, the MRI signal only depends indirectly on the tissue's  $T_1$ -value, and further processing is necessary to estimate the value of  $T_1$ .  $T_1$ -mapping is done by scanning the tissue several times with the FSPGR sequence, each time with a different flip angle. Then, the  $T_1$ -value can be estimated in each voxel by fitting eq. (2.5) to the measured signal values. This method is called the Variable Flip Angle method.

### 2.4.2 Inversion Recovery

The Inversion Recovery (IR) sequence is another frequently used method for  $T_1$ -mapping. The IR sequence starts with an inversion pulse (180 degrees), followed by a wait time  $TI$ . During the wait time, the longitudinal magnetization begins to recover. Then, a 90 degrees pulse is applied, after which an echo is immediately acquired. Finally, the spins are allowed to relax back to equilibrium. The sequence is then repeated using different  $TI$ s. The amount of recovery during the wait time, and thus the signal amplitude, depends on the  $T_1$  value of the sample:

---

<sup>3</sup> The number of pulses depends on the flip angle and repetition time. This topic is addressed in detail in Chapter 4.



$$S = M(1 - 2\exp(-TI/T_1)) \quad (2.6)$$

where  $M$  is a composite factor that reflects the proton density and the gain factor of the scanner. Fitting equation (2.6) to the measured signals in each voxel then gives an estimate of the  $T_1$  value.

The IR method provides a very reliable  $T_1$ -map, but the sequence is very slow (3 to 4 minutes per TI). This means that it is not suitable for imaging moving objects, and it is also not viable in a clinical setting.

## 2.5 Contrast Agents

In MRI, contrast agents are intravenously delivered substances that increase contrast between different tissues. The most commonly used MRI contrast agents are gadolinium(III) chelates. Gadolinium(III) is used, as it is strongly paramagnetic, having seven unpaired electrons in the outer shell. Chelates are hydrophilic cage structures with the gadolinium(III) ion trapped inside, and are used to ensure that the toxic gadolinium is not metabolised by the body. The gadolinium(III) chelates interact with nearby hydrogen atoms in two ways (2).

First, the chelates have one or more docking sites, where water molecules can reside. When one of the hydrogen atoms of a water molecule gets near the gadolinium(III) ion, the hydrogen nucleus will couple to unpaired electrons in the outer shell of the gadolinium ion. This allows the hydrogen nucleus to transition to the equilibrium state (aligned with the magnetic field) more quickly, thus decreasing the  $T_1$  time (3). Secondly, the contrast agent disturbs the local magnetic field slightly, causing the transverse components of the spins to disperse more quickly, thereby reducing the  $T_2$  and  $T_2^*$  times.

The change in  $T_1$ ,  $T_2$ , and  $T_2^*$  depends on the concentration of contrast agent, and on the relaxivity ( $R_1$ ,  $R_2$ ,  $R_2^*$ ) of the contrast agent. For most contrast agents, this follows the inverse linear relationships:

$$\frac{1}{T_1} = \frac{1}{T_{10}} + R_1 \cdot C \quad ; \quad \frac{1}{T_2} = \frac{1}{T_{20}} + R_2 \cdot C \quad ; \quad \frac{1}{T_2^*} = \frac{1}{T_{20}^*} + R_2^* \cdot C, \quad (2.7)$$

with  $T_{x0}$  the respective relaxation time in the absence of contrast agent, and  $C$  the contrast agent concentration. Contrast agents have the most influence on  $T_1$ , and are thus mostly used for  $T_1$ -weighted scans. This is because  $T_{10} > T_{20} > T_{20}^*$ , while the relaxivities are comparable. Because of this, contrast agents are commonly used to increase the image contrast of  $T_1$  weighted scans, such as in DCE-MRI. Note that both equations (2.5) and (2.7) are nonlinear. This nonlinearity must be taken into account when the contrast agent concentration is to be computed accurately from an FSPGR based MRI signal.

## 2.6 DCE-MRI and Pharmacokinetic Modelling

Dynamic Contrast Enhanced MRI is a method to visualize dynamic, physiological properties of tissues, by monitoring the tissue's response to an intravenous injection of contrast agent. It consists of a series of fast MRI scans that are acquired in a period of several minutes, during which a gadolinium-based contrast agent bolus is being injected. This results in the tissues changing their signal intensity in time, in a fashion which is dependent on the tissue microvascularization. The technique has proven to be valuable in the detection and staging of cancer (4), and the assessment of various inflammatory diseases (5).

In principle, the diagnosis and staging can be done on the basis of the visual assessment of the series of DCE images, without further processing. However, with an appropriate analysis, DCE-MRI can provide quantitative parameters that are directly related to the intrinsic physiological properties of tissues. This is done by formulating a model which describes how the MRI signal changes as a result of the tissue's reaction to the contrast agent, and then fitting this model to the measured DCE-MRI data. The complete model therefore includes a physiological (pharmacokinetic) component (e.g., how the contrast agent leaks out of the capillaries), and a physical component (i.e., how the contrast agent affects the MRI signal). Several pharmacokinetic models exist, to model various tissue types,

different organs, and types of contrast agent (6). This thesis focuses on tissues with simple characteristics (i.e., only concentration differences and diffusion drive the exchange of contrast agent between two compartments), which permits the use of the Tofts' pharmacokinetic model.

### 2.6.1 Tofts' Model

Tofts' model is a pharmacokinetic model describing how tissues react to the presence of contrast agent in their feeding artery (7,8). It assumes that a voxel of tissue is comprised of three compartments: cells, plasma and interstitial space. The contrast agent arrives through the blood plasma, and it will diffuse into the interstitial space through pores in the capillary walls, driven by the difference in contrast agent concentration. Eventually, the contrast agent will diffuse out of the tissues again, finally to be excreted by the kidneys. See Figure 2.5 for a schematic overview of Tofts' Model.

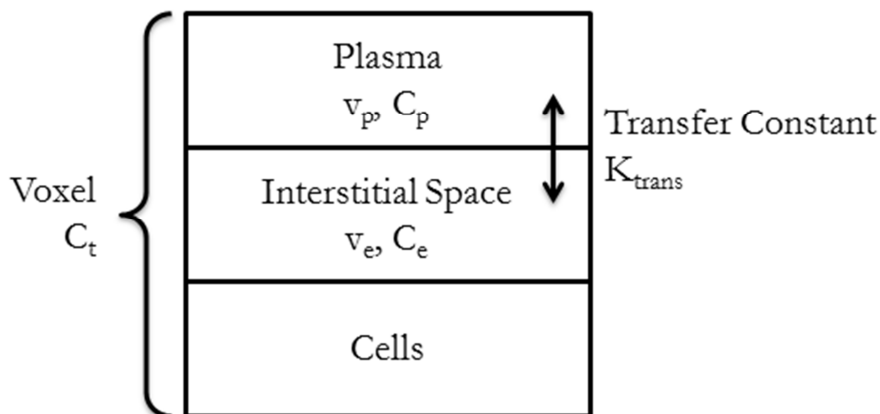


Figure 2.5: Schematic overview of Tofts' Model.

It is assumed that the cells do not interact with the contrast agent, and that the contrast agent in the plasma is replenished quickly enough to not affect the contrast agent concentration. Furthermore, the rate of diffusion of contrast agent between the plasma and interstitial space is driven by the difference in concentration, and is expressed by a transfer constant  $K_{trans}$ . In Tofts' model,  $K_{trans}$  depends on the type of contrast agent and the degree of vessel wall permeability. Under the condition of adequate flow of contrast agent and limited permeability, it is defined as the product of the capillary permeability, the capillary wall surface area, and the tissue

density. Hence, an increased  $K_{\text{trans}}$  may indicate damage to the capillary wall, or swelling of the tissue, as the result of some pathology.

For the entire voxel, the concentration is described by:

$$\begin{aligned} C_t(t) &= v_p \cdot C_p(t) + v_e \cdot C_e(t) \\ v_e \frac{dC_e(t)}{dt} &= K_{\text{trans}} (C_p(t) - C_e(t)) \end{aligned} \quad (2.8)$$

where  $C_p$ ,  $C_e$  and  $C_t$  are the contrast agent concentration in the plasma, interstitial space and the tissue respectively, and  $v_p$  is the fractional volumes of the plasma compartment. The solution of this set of equations is:

$$C_t(t) = v_p \cdot C_p(t) + K_{\text{trans}} \int_0^t C_p(\tau) \exp(-K_{\text{ep}}(t-\tau)) d\tau, \quad (2.9)$$

with  $K_{\text{ep}} = K_{\text{trans}}/v_e$ . Hence, with the knowledge of the contrast agent concentration in the tissue ( $C_t(t)$ ) and the contrast agent concentration in the feeding artery ( $C_p(t)$ ), the pharmacokinetic tissue properties ( $v_p$ ,  $v_e$ ,  $K_{\text{ep}}$  and  $K_{\text{trans}}$ ) can be determined.

The tissue properties can be determined on a voxel by voxel basis, in order to assess the tissue integrity locally, though the results may be susceptible to noise on the input concentrations. Alternatively, the tissue properties may be determined from the average tissue concentration of a larger region of interest, increasing the robustness, but at the cost of resolution.

Importantly, the concentration of contrast agent in the tissue  $C_t(t)$  cannot be measured from the MRI signal directly, but needs to be inferred from the intrinsic  $T_1$ -time of the tissue before and during contrast delivery, using equation (2.7). This makes the model not only dependent on the assumptions mentioned above, but also on the accuracy of the calculation of the  $T_1$ -time. Moreover, the contrast agent concentration in the plasma (the arterial input function) also plays an essential role in the model (eq. (2.9)). The plasma concentration is difficult to measure, and any error in its calculation is propagated through the model and into the calculated

model parameters. For this reason, it is necessary that both the  $T_1$ -time of the tissue and the arterial input function are determined accurately.

## 2.7 References

1. Haacke E, Cheng Y, Brown R, Thompson M, Venkatesan R. *Magnetic Resonance Imaging: Physical Principles and Sequence Design* 2014.
2. De Leon-Rodriguez LM, Martins AF, Pinho MC, Rofsky NM, Sherry AD. Basic MR relaxation mechanisms and contrast agent design. *Journal of magnetic resonance imaging : JMRI* 2015;42(3):545-565.
3. Caravan P, Ellison JJ, McMurry TJ, Lauffer RB. Gadolinium(III) Chelates as MRI Contrast Agents: Structure, Dynamics, and Applications. *Chemical reviews* 1999;99(9):2293-2352.
4. Sung YS, Kwon HJ, Park BW, Cho G, Lee CK, Cho KS, Kim JK. Prostate cancer detection on dynamic contrast-enhanced MRI: computer-aided diagnosis versus single perfusion parameter maps. *AJR American journal of roentgenology* 2011;197(5):1122-1129.
5. Tielbeek JA, Ziech ML, Li Z, Lavini C, Bipat S, Bemelman WA, Roelofs JJ, Ponsioen CY, Vos FM, Stoker J. Evaluation of conventional, dynamic contrast enhanced and diffusion weighted MRI for quantitative Crohn's disease assessment with histopathology of surgical specimens. *European radiology* 2014;24(3):619-629.
6. Sourbron SP, Buckley DL. Classic models for dynamic contrast-enhanced MRI. *NMR in biomedicine* 2013;26(8):1004-1027.
7. Tofts PS, Brix G, Buckley DL, Evelhoch JL, Henderson E, Knopp MV, Larsson HB, Lee TY, Mayr NA, Parker GJ, Port RE, Taylor J, Weisskoff RM. Estimating kinetic parameters from dynamic contrast-enhanced T(1)-weighted MRI of a diffusible tracer: standardized quantities and symbols. *Journal of magnetic resonance imaging : JMRI* 1999;10(3):223-232.
8. Tofts PS. T1-weighted DCE imaging concepts:Modelling, acquisition and analysis. *MAGNETOMFlash* 2010(3):30-39.

# 3 Feasibility of a Fast Method for $B_1$ -Inhomogeneity Correction for FSPGR Sequences

---

## *Abstract*

The Fast Spoiled Gradient Echo (FSPGR) sequence is often used in MRI to create  $T_1$ -weighted images. The signal intensity generated by this sequence depends on the applied flip angle. Knowing the correct flip angle is essential for the determination of  $T_1$ -maps by means of an FSPGR based Variable Flip Angle (VFA) approach. Also, quantitatively determining the concentration of contrast agent in case of Dynamic Contrast Enhanced MRI (DCE-MRI) requires knowledge of the applied flip angle. In both cases, the  $B_1$ -field (in)homogeneity significantly affects the results. In this paper, we present a new method to obtain both the  $T_1$ -map and  $B_1$ -inhomogeneity map using scans that can each be acquired within a breath-hold. We combine two short sequences for  $T_1$  quantification: Variable Flip Angle and Look-Locker (LL). The  $T_1$ -maps obtained from the LL data were used to estimate the  $B_1$ -inhomogeneity inherently present in the VFA data, which was then used to correct for the VFA method's inaccurate flip angles. This way, a reliable  $T_1$ -map could be computed, which was validated using both in vitro and in vivo scans. The in vitro results show that the procedure yields a substantially smaller mean deviation in  $T_1$  from the  $T_1$  measurement's gold standard (the Inversion Recovery method), while the in vivo results show both a more accurate estimation of  $T_1$  and a reduction of the influence of the  $B_1$ -inhomogeneity on the signal intensity.

*As published in:* JJN van Schie et al., "Feasibility of a fast method for  $B_1$ -inhomogeneity correction for FSPGR sequences.", Magn Reson Imaging. 2015 Apr;33(3):312-8.

### **3.1 Introduction**

The Fast Spoiled Gradient Echo sequence is a widely used MRI technique, able to produce  $T_1$ -weighted images within seconds. It lies at the basis of the Variable Flip Angle (VFA) method, which is used to estimate a tissue's  $T_1$ -value. It is also employed in Dynamic Contrast Enhanced MRI (DCE-MRI), a technique which visualizes the response of tissues to the inflow of a contrast agent. As the inflow and subsequent outflow of the contrast agent reflects the integrity of the tissue's vascularization, DCE-MRI is especially useful for increasing the specificity in tissue characterization, staging of the local extent of disease and biopsy planning, monitoring preoperative chemotherapy and detection of recurrence (1-5). The signal intensity of an FSPGR sequence depends directly on the flip angle used. It is essential to know the exact flip angle in order to make quantitative measurements of the  $T_1$ -value in an FSPGR based VFA method. For the case of pharmacokinetic modelling with DCE-MRI, it is needed in order to calculate the tissue contrast agent concentration reliably (6). Because of its dependence on the flip angle, the FSPGR sequence is inherently sensitive to  $B_1$ -inhomogeneity effects. In this paper, a new method is proposed for simultaneous  $T_1$ -mapping and  $B_1$ -field correction by an advanced post-processing technique. The employed MRI sequences are each acquired within a breath-hold.

#### **3.1.1 Related Work**

A common method, and currently the gold standard, to estimate the longitudinal relaxation time ( $T_1$ ) of a tissue of interest is the Inversion Recovery method (IR) (7). Despite the fact that it produces  $T_1$ -maps with high resolution and signal-to-noise ratio (SNR), this method is impractical for some applications due to its long scan time.

A modification of IR is the Look-Locker (LL) method (8). It uses an inversion pulse similar to that of IR, followed by quickly repeated small flip angle pulses. The signal is acquired after each pulse, thus sampling the spins' longitudinal magnetization as it relaxes back to equilibrium. The longitudinal relaxation rate is slightly perturbed by the pulse train, which is accounted for in the final  $T_1$

calculation. The Look-Locker method has a much shorter acquisition time than IR and is, just like IR, almost insensitive to space-variant B<sub>1</sub>-attenuation effects (less than 5% deviation of T<sub>1</sub> for realistic settings (9)). The downside, however, is that if a short acquisition time per volume is needed, both the SNR and the resolution can be quite low.

Another method to estimate the T<sub>1</sub>-map is the Variable Flip Angle (VFA) method (10). VFA acquires images using a series of FSPGR sequences with varying flip angles. The theoretical signal relation is then fitted to the acquired signal, providing a T<sub>1</sub>-map. However, the applied flip angle strongly depends on the exact strength of the B<sub>1</sub>-field, making the technique very sensitive to any B<sub>1</sub>-field inhomogeneity, which, if present, can result in a biased estimation of T<sub>1</sub>. The inherently inhomogeneous nature of the B<sub>1</sub>-field complicates automatic correction of the flip angle.

A method to compute a B<sub>1</sub>-inhomogeneity map independently of T<sub>1</sub> is to use VFA with flip angles around 180 degrees (11). Since a signal null should occur at 180 degrees, any deviation from 180 degrees can be attributed to B<sub>1</sub>-inhomogeneity effects. This method is not easily applicable in clinical practice, due to the high energy deposition associated with high flip angle FSPGR sequences (the energy deposition increases quadratically with the flip angle). Alternatively, the B<sub>1</sub>-inhomogeneity can be calculated with the Double Angle method (12). This method uses two FSPGR sequences, the second using double the flip angle of the first, and employs trigonometric relations to estimate the B<sub>1</sub>-inhomogeneity. The latter method requires a long scan time, which can be undesirable in clinical practice, especially when the scan must be acquired during a breath-hold. Furthermore, specialized methods such as the Actual Flip Angle Imaging (AFI) method (13) and the DREAM method (14) exist. They make use of specially tailored pulse sequences, designed such that a B<sub>1</sub>-inhomogeneity map can be calculated from the acquired signal. The AFI method again requires a long scan time, and thus cannot be done within a breath-hold. The DREAM approach is much faster, and produces good B<sub>1</sub>-inhomogeneity maps, but this has only been tested on a 3T scanner.



Generally, such specialized methods are less often available on clinical scanners without a research mode or sequence-developing capabilities.

### **3.1.2 Objective**

This article aims to study the feasibility of a fast method to simultaneously obtain an accurate pre-contrast T<sub>1</sub>-map as well as a B<sub>1</sub>-inhomogeneity map. This is done by combining two short scans: (1) a coarse Look-Locker based T<sub>1</sub>-scan, and (2) a VFA based T<sub>1</sub> quantification. In fact, a low resolution T<sub>1</sub>-map, acquired with the LL method, serves to correct the flip angle inaccuracies in a high resolution VFA T<sub>1</sub>-map. As a result, the T<sub>1</sub>-map and the corrected flip angle can be used together, for example in computing accurate contrast agent concentration profiles from DCE-MRI data, for quantitative pharmacokinetic analysis.

## **3.2 Methods**

The presented technique to compute the T<sub>1</sub>- and B<sub>1</sub>-inhomogeneity maps involves two MRI scans: one series of FSPGR sequences for the VFA method, and one LL sequence. All scans were made with a 1.5 T MRI scanner (Siemens Avanto).

### **3.2.1 Experimental Material**

The method was first applied in vitro to a home-built phantom consisting of ten vials, each having a diameter of 3 cm. All but one vial contained an aqueous solution with varying concentrations of Gd-DTPA (Magnevist, Bayer Schering Pharma, Berlin, Germany) as well as a gelling agent (agar) to suppress free water movement. The remaining vial contained air. All vials were mounted in a plastic box filled with water doped with copper sulphate to reduce its T<sub>1</sub>- and T<sub>2</sub>-times. For reference, the ten vials are labelled 1 to 10 column-wise, starting at the top-left corner (see Figure 3.1, left). Second, the same method was employed in vivo, on a healthy human male volunteer. The pelvic region was selected as the region of interest. In this region, the body movement due to breathing is minimal, while several different types of tissue (muscle, fat, bone) are present. The absence of

movement allowed to obtain a reference  $T_1$ -map by means of the Inversion Recovery method (see below), which is not easily achievable in moving body parts (e.g., in the upper parts of the abdomen). Third and last, the method was employed on a second healthy human male volunteer, with the central abdominal region selected as the region of interest. Since this region is affected by breathing motion, each scan was made during a period of breath-hold. As a pre-processing step, all breath-hold volumes were registered to each other using an in-house registration algorithm based on the autocorrelation of local structures (15).

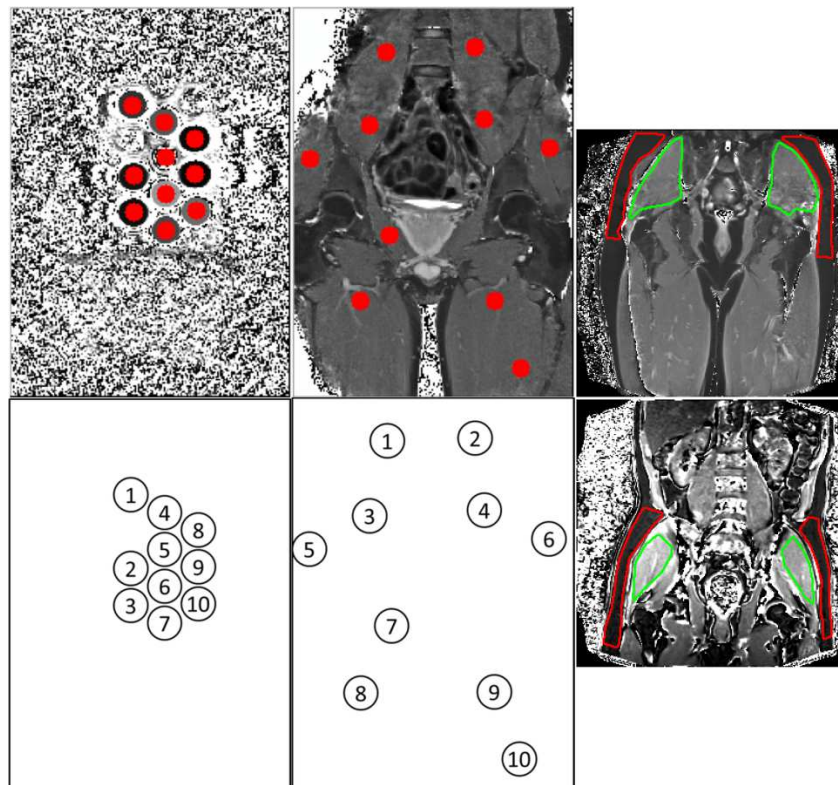


Figure 3.1: Left column: positioning and labelling of the ROIs in the 10 vials. Middle column: positioning and labelling of the ROIs in the first human volunteer. Right column: positioning of ROIs in the second human volunteer, for IR (top) and VFA/LL (bottom). Red contains fat tissue, green contains muscle tissue.

### 3.2.2 Look-Locker $T_1$ -map

The first step in the proposed method was to obtain a low-resolution  $T_1$ -map. The subjects were scanned with a 2D Look-Locker sequence: an inversion pulse followed by eight small flip angle pulses of  $\alpha = 8$  degrees each, spaced by intervals of

$\tau = 98$  ms (phantom and first volunteer), or  $\tau = 80$  ms (second volunteer), and a repetition time of 3000 ms. The phantom and first volunteer were scanned with a matrix size of  $128 \times 104$  pixels, seven slices (FOV:  $400 \times 325 \times 30$  mm<sup>3</sup>, slice thickness = 2.5 mm), for a scan duration of 20 seconds per slice. The second volunteer was scanned with a matrix size of  $128 \times 128$  pixels, six slices (FOV:  $450 \times 450 \times 24$  mm<sup>3</sup>, slice thickness = 4 mm), for a scan duration of 18 seconds per slice.

The signal strength of a LL scan follows the theoretical relation:

$$S = \left| A \left( 1 - B \exp(-\tau/T_1^*) \right) \right|, \quad (3.1)$$

with

$$\frac{1}{T_1^*} = \frac{1}{T_1} - \frac{\ln(\cos(\alpha))}{\tau}. \quad (3.2)$$

This relation was fitted to the measured signal, using a maximum likelihood estimation algorithm, based on a Rician noise model. This results in estimates for  $A$ ,  $B$ , and in particular,  $T_1$ . This algorithm is part of an in-house software package (16) implemented in Matlab (MathWorks, Massachusetts, USA).

### **3.2.3 Variable Flip Angle T<sub>1</sub>-map**

Next, the subjects were scanned with a Variable Flip Angle protocol. This protocol consisted of five FSPGR sequences using flip angles  $\alpha$  of 1, 3, 5, 7 and 9 degrees respectively, with TR = 4.74 ms and TE = 2.38 ms. The phantom and first volunteer were scanned with a matrix size of  $256 \times 184 \times 36$  voxels (FOV:  $400 \times 288 \times 90$  mm<sup>3</sup>, scan duration: 7 s per volume), the second volunteer was scanned with a matrix size of  $256 \times 256 \times 36$  voxels (FOV:  $450 \times 450 \times 144$  mm<sup>3</sup>, scan duration: 7 s per volume). The repetition time was chosen to keep the total scan duration short, while the range of flip angles was chosen to ensure that the tissue's expected Ernst angle would likely fall inside this range. The theoretical relation for the signal strength  $S$  in FSPGR imaging, including a B<sub>1</sub>-inhomogeneity factor  $\zeta$ , is given by (10):

$$S = \frac{N \sin(\zeta\alpha) \left(1 - \exp\left(-\frac{T_R}{T_1}\right)\right)}{1 - \cos(\zeta\alpha) \exp\left(-\frac{T_R}{T_1}\right)}. \quad (3.3)$$

The VFA  $T_1$ -map was obtained by fitting eq. (3.3) to the five FSPGR images while assuming absence of inhomogeneities ( $\zeta = 1$ ).

### 3.2.4 $B_1$ -inhomogeneity map and VFA $T_1$ -map

Observe that the flip angle  $\alpha$  is assumed to be linearly dependent on the  $B_1$  variation (9). In order to determine  $\zeta$ , eq. (3.3) was fitted to the acquired VFA images (voxel by voxel), using the  $T_1$ -map obtained with the LL method for  $T_1$ , and  $\zeta$  and  $N$  as free parameters. In other words, the amount of  $B_1$ -variation was estimated by checking how much the flip angles needed to be adjusted in order for the VFA method to produce the same  $T_1$  as the LL method.

The initial  $\zeta$ -map thus obtained is noisy due to the involvement of the LL  $T_1$ -map. The real  $\zeta$ -map is, based on principles of physics, expected to be smoothly varying. Hence, we fitted a low-order polynomial to the data: a second order polynomial to the vials, a fourth order polynomial in the first volunteer study, and a sixth order polynomial in the second volunteer study, to match the expected amount of structure in the region of interest within the FOV in each case. Essentially this extracts the global trend. This trend derived from the initial  $\zeta$ -map is not affected by the local signal fluctuations, since the latter cancel out while fitting a global function. The fitting was performed by means of weighted least squares regression, reinforcing the robustness by excluding outliers based on the confidence in the corresponding  $\zeta$  factor. Essentially, the weights determined which points were taken into account in the fitting.

In the in vitro case, the area outside the vials was manually segmented and its confidence weight was set to 0. In this way, artifacts (points residing in the air and water outside the vials) were discarded. In the in vivo cases, the background was segmented by thresholding the amplitude factors of the LL scan ( $A$  in eq. (3.1)) and the VFA scan ( $N$  in eq. (3.3)), and the weight set to 0. Subsequently, the

confidence was determined based on statistical grounds and prior knowledge. Particularly, if  $\zeta$  fell outside the range of a factor of two geometric standard deviations from its geometric mean, or if the corresponding  $T_1$  fell outside a physically expected range of 10 to 2000 ms, the weight was set to 0; otherwise it was set to 1. A geometric metric (instead of a ‘regular’ arithmetic one) was used, since the  $B_1$ -inhomogeneity is assumed to have a multiplicative effect (9). The former condition served to exclude statistically unreliable points due to extreme noise on the LL data; the latter condition aimed to discard physically infeasible measurements. The resulting  $\zeta$ -map after fitting served as the final  $B_1$ -inhomogeneity map.

Finally, equation (3.3) was fitted to the measured VFA data using the fitted  $B_1$ -inhomogeneity map as fixed  $\zeta$ , with  $T_1$  and  $N$  as free parameters. Essentially, the fitted  $\zeta$ -map compensated for the  $B_1$ -effects normally present when using the VFA method. Herewith, the corrected VFA  $T_1$ -map was obtained.

Note that the larger pixel sizes in the LL data make that pixels contain multiple tissues. These so-called partial volume effects occur predominantly at boundaries between tissues, and produce erroneous values for  $\zeta$ : too high for one tissue, and too low for the other. Such voxels are discarded as outliers. Generally, the number of voxels near boundaries is small compared to the total number of included voxels. Hence, the effect they have on the final outcome after regression with a low-order polynomial is negligible.

### 3.2.5 Inversion Recovery, reference $T_1$ -mapping

For the phantom and first volunteer, a reference  $T_1$ -map was acquired using an Inversion Recovery scan. The region of interest was scanned six times, each with a repetition time of 7000 ms, inversion times of 50, 150, 300, 600, 1500 and 2000 ms respectively, and a matrix size of  $256 \times 184 \times 18$  voxels (FOV:  $400 \times 288 \times 85$  mm<sup>3</sup>, slice thickness: 2.5 mm). The duration of each scan was 275 s, bringing the total IR scan time to 27.5 minutes. A mono-exponential recovery curve was fitted to the measured intensities, providing a  $T_1$ -map to be used as gold standard. The theoretical relationship between the IR signal and  $T_1$  is similar to equation (3.1),

but with a fixed  $B = 2$  and with  $T_1^* = T_1$ . For the second volunteer, breathing motion made the use of a lengthy Inversion Recovery scan infeasible in the upper abdominal region. Instead, a scan of the lower abdomen was performed to get the IR reference  $T_1$ -map, using the same inversion times. In this case, the repetition time was 6700 ms, and the matrix size was set to  $256 \times 256 \times 18$  voxels (FOV:  $450 \times 450 \times 136$  mm<sup>3</sup>, slice thickness: 4 mm).

### 3.2.6 Statistical Analysis

A circular ROI, 20 mm in diameter, was manually positioned inside each of the vials in the reference IR scan (see Figure 3.1, left column). Likewise, ten circular regions, 20 mm in diameter, were drawn at representative, homogeneous positions in the IR scan of the first volunteer (see Figure 3.1, middle column). The data from these in vitro and in vivo experiments were separately analysed. The average  $T_1$ -values from the uncorrected VFA, the corrected VFA and the LL scans in each region were compared to the average  $T_1$ -values estimated from the IR scan by means of a two-tailed, paired t-test. Subsequently, the pooled variance of the ROIs was calculated. The pooled variances from the uncorrected VFA, the corrected VFA and the LL scans were compared to the pooled variance from the IR scan by means of an F-test. For the second volunteer study, regions of fat and muscle tissue were manually segmented in the VFA  $T_1$ -map of the upper abdomen, and the IR  $T_1$ -map of the lower abdomen. The regions were chosen to lie in the overlapping area. The mean  $T_1$ -values of these regions were then compared to each other with a z-test. In all cases, a p-value  $< 0.05$  was considered to indicate a significant difference.

## 3.3 Results

### 3.3.1 In vitro $T_1$ -maps

The  $T_1$ -maps made using IR, LL, uncorrected and corrected VFA are shown in Figure 3.2a-d respectively. Notice the lower resolution (larger pixel sizes) and increased noise (e.g., vials 3, 6, 10) of the LL  $T_1$ -map (Figure 3.2b). Additionally,

observe that the uncorrected VFA  $T_1$ -map shows an underestimation of the  $T_1$ -values compared to the IR  $T_1$ -map (e.g., compare vial 6 in Figure 3.2a and c).

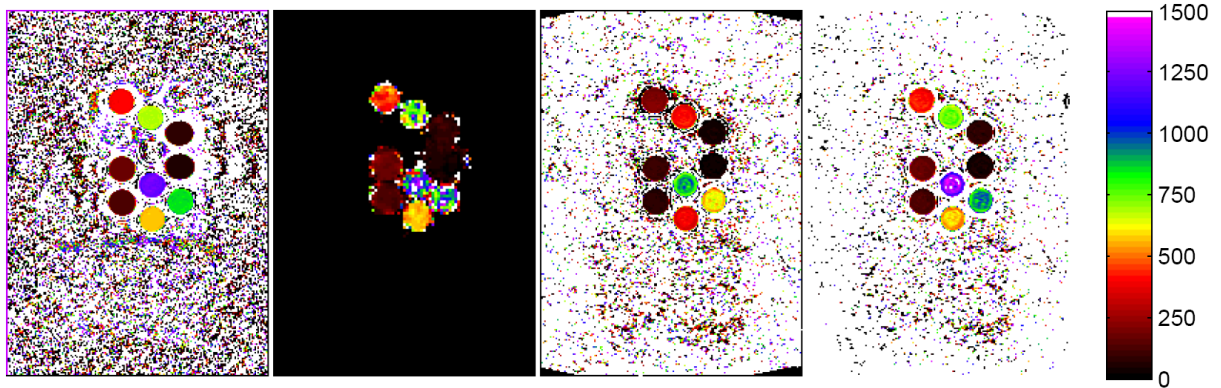


Figure 3.2:  $T_1$ -maps of the phantom obtained with: (a) Inversion Recovery; (b) Look-Locker; (c) uncorrected Variable Flip Angle; (d) corrected Variable Flip Angle. Units are [ms]. FOV:  $400 \times 288 \text{ mm}^2$ .

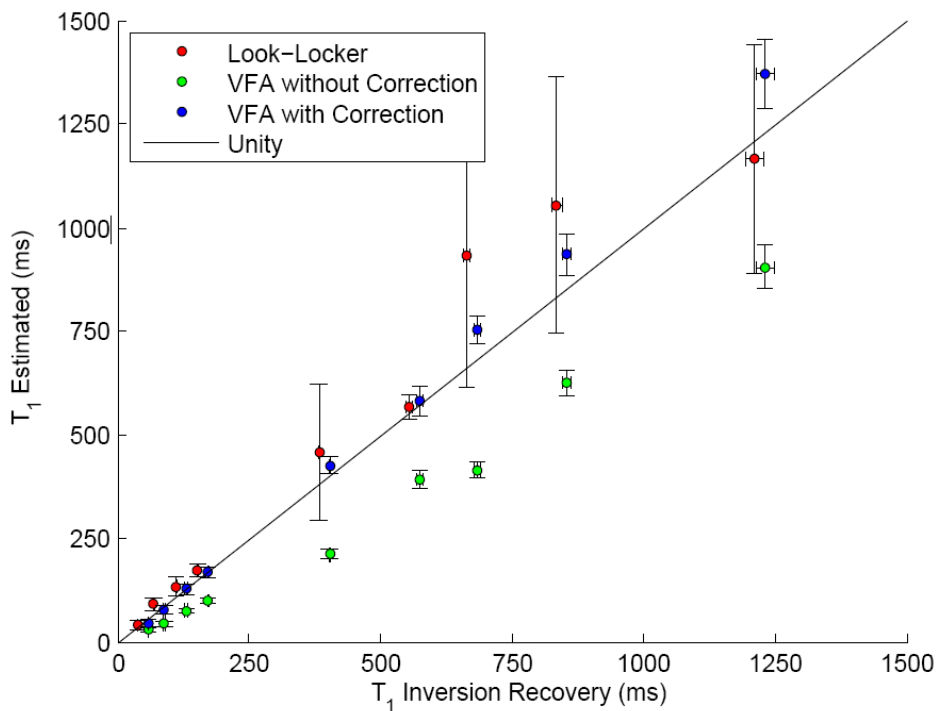


Figure 3.3: Comparison of  $T_1$  estimation methods in vitro. The data points denote the mean  $T_1$  inside circular ROIs (6 pixel radius, 1 slice thick) in the centres of each vial. The error bars denote one standard deviation. The data points (from left to right) correspond to vials: 9, 8, 3, 2, 1, 7, 4, 10 and 6. For clarity, the data points from the LL method have been shifted slightly to the left, as to prevent occlusion by other data points.

A comparison of the  $T_1$  values in the ROIs estimated by the four methods is shown in Figure 3.3, using the  $T_1$  values found with Inversion Recovery as reference standard. Estimating the  $T_1$ -value of vial 5 (containing air) failed with each method. Therefore, a meaningful comparison could not be made, and vial 5 was excluded from further analysis.

The mean difference from IR and the root mean (pooled) variance of each method, both averaged over the vials, are shown in Table 3.1. The average  $T_1$ -values from the proposed method did not differ significantly from the IR values ( $p = 0.099$ ). The estimated  $T_1$ -values of the uncorrected VFA scan differed significantly from IR ( $p = 0.003$ ). Comparing the four methods' variances, averaged over the nine included vials, all differed significantly from each other ( $p < 0.05$ ), with the exception of the variances of the uncorrected and corrected VFA ( $p = 0.18$ ).

Table 3.1: Comparison of the four used methods for  $T_1$  quantification in vitro showing the mean difference (MD) from the reference method (IR), as well as each method's root mean variance (RMV), both averaged over the vials.

<b>Method</b>	<b>MD (ms)</b>	<b>RMV (ms)</b>
IR	0.000	7.005
LL	46.98	183.0
VFA (uncorrected)	-155.5	23.53
VFA (corrected)	32.61	37.54

### **3.3.2 In vitro B<sub>1</sub>-inhomogeneity maps**

The initial  $\zeta$  map obtained by fitting eq. (3.3) in each pixel is shown in Figure 3.4a. The mean value for  $\zeta$  inside the regions of interest was 79.3%, with a standard deviation of 10.7%. The binary weights that were used in the fitting of the low-order polynomial are shown in figure 4b. Observe that several points considered unreliable occur within the vials. These points are discarded due to noise on the LL data. After fitting the low order polynomial to the B<sub>1</sub>-inhomogeneity map (Figure 3.4c), the mean value for  $\zeta$  inside the vials is almost the same as before (77.4%), but the standard deviation has decreased to 0.7%.



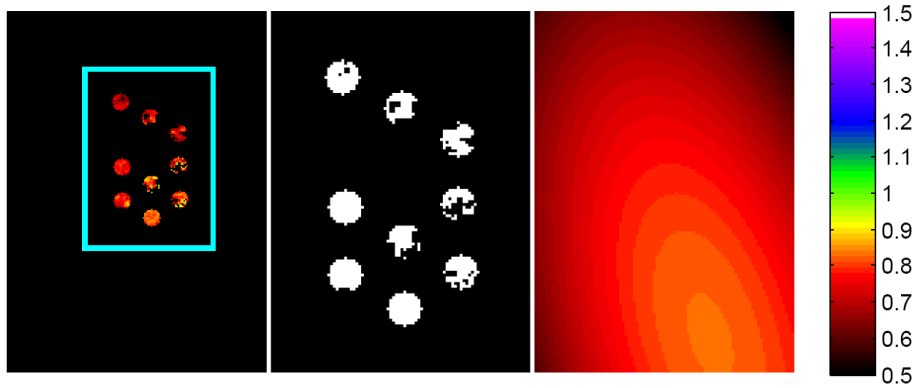


Figure 3.4:  $B_1$ -inhomogeneity map of the phantom. FOV:  $400 \times 288 \text{ mm}^2$ . (b) Binary weight map used for fitting (black = 0, white = 1). (c) Fitted  $B_1$ -inhomogeneity map. Images (b) and (c) are zoomed in to the rectangular area displayed in (a); FOV:  $200 \times 144 \text{ mm}^2$ .

### 3.3.3 In vivo $T_1$ -maps

The  $T_1$ -maps made using IR, LL, uncorrected and corrected VFA of the first volunteer study are shown in Figure 3.5. Notice that the uncorrected VFA  $T_1$ -map shows a spatially varying value for  $T_1$ , i.e. the values increase from the image border inwards (indicated by the arrows), which is not seen on the IR  $T_1$ -map. This reflects the location dependency of the  $\zeta$ -factor. Also, there is a global underestimation of the  $T_1$ -value obtained with the uncorrected VFA method, as the colours are generally darker (lower  $T_1$ -values).

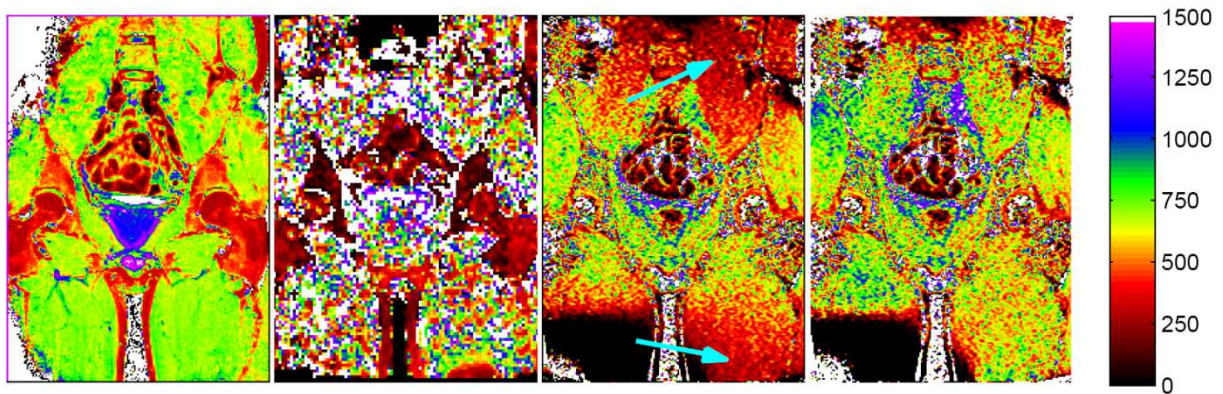


Figure 3.5:  $T_1$ -maps of a human male pelvis obtained with: (a) Inversion Recovery; (b) Look-Locker; (c) uncorrected Variable Flip Angle; (d) corrected Variable Flip Angle. FOV:  $450 \times 450 \text{ mm}^2$ .

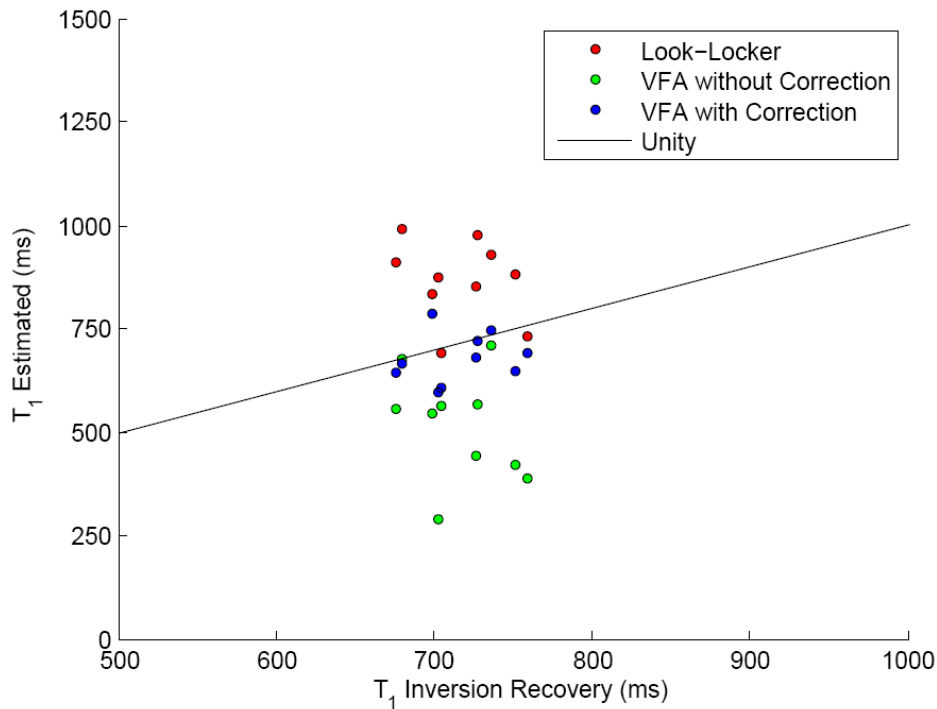


Figure 3.6: Comparison of  $T_1$  estimation methods in vivo. The data points denote the mean  $T_1$  inside circular ROIs (6 pixel radius, 1 slice thick). Error bars have been omitted for clarity; an indication of the variance per method is shown in Table 3.2.

Table 3.2: Comparison of the four used methods for  $T_1$  quantification in vivo, showing the mean difference (MD) from the reference method (IR), as well as each method's root mean variance (RMV), both averaged over the ROIs.

Method	MD (ms)	RMV (ms)
IR	0.000	57.09
LL	150.8	438.7
VFA (uncorrected)	-199.0	95.08
VFA (corrected)	-37.33	127.6

A comparison of the  $T_1$ -values in the ROIs estimated by the four methods is shown in Figure 3.6, again using the  $T_1$  values from IR as the reference standard. The mean difference from IR and the root mean (pooled) variance of each method, both averaged over the vials, are collated in Table 3.2. The average  $T_1$ -values from the proposed method did not differ significantly from the IR values ( $p > 0.084$ ). The estimated  $T_1$ -values of the uncorrected VFA as well as the LL scan did differ

significantly from IR ( $p = 0.0016$ ,  $p = 0.0017$  respectively). The four methods' variances, averaged over the 10 ROIs, all differed significantly from each other ( $p < 0.05$ ), with the exception of the variances of the uncorrected and corrected VFA ( $p = 0.37$ ), and the variances of the uncorrected VFA and IR ( $p = 0.12$ ).

For the second volunteer study, the reference  $T_1$ -map of the lower abdomen is shown in Figure 3.7a. The  $T_1$ -maps of the upper abdomen, obtained with the other three methods, are shown in Figure 3.7b-d. The location of the IR  $T_1$ -map was chosen to be different from the other three methods, because the presence of breathing motion makes a lengthy IR scan infeasible in the upper abdomen. The mean  $T_1$ , standard deviation, and median  $T_1$  of both muscle tissue and fat tissue are shown in Table 3.3.

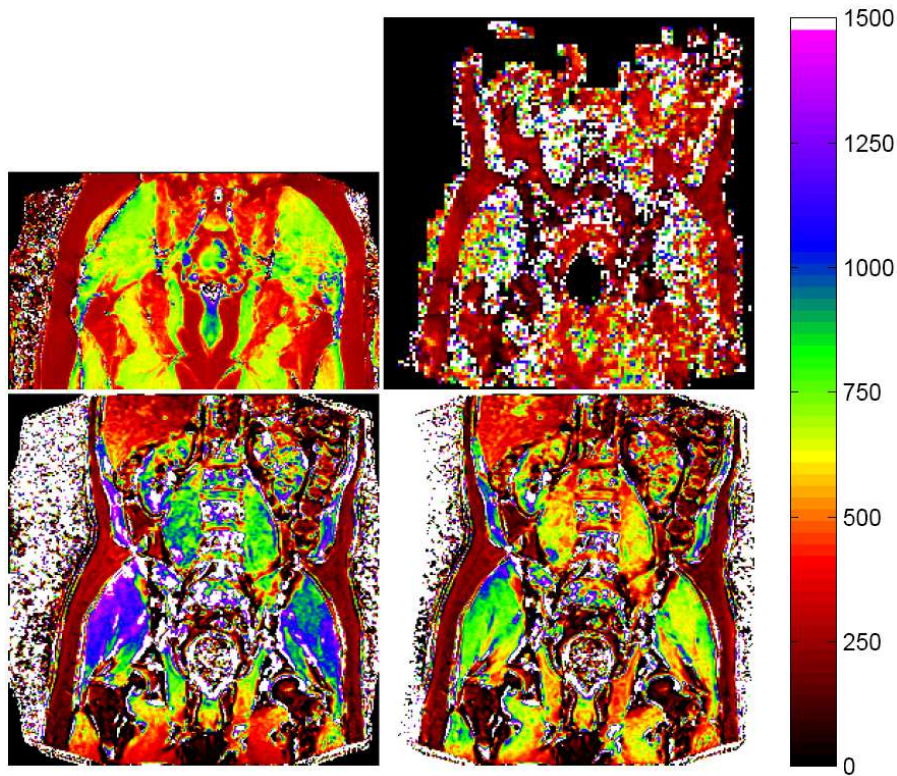


Figure 3.7:  $T_1$ -maps of a human male lower and upper abdomen, obtained with: (a) Inversion recovery (lower abdomen); (b) Look-Locker (upper abdomen); (c) uncorrected Variable Flip Angle (upper abdomen); (d) corrected Variable Flip Angle (upper abdomen). Note that the  $T_1$ -map in (a) is shifted downwards to match the anatomy of the other three  $T_1$ -maps. FOV:  $450 \times 450$  mm<sup>2</sup>.

Table 3.3: Comparison of T<sub>1</sub> values estimated by IR, LL, uncorrected and corrected VFA, for muscle and fat tissue.

Method	Muscle tissue T <sub>1</sub> (ms)			Fat tissue T <sub>1</sub> (ms)		
	Mean	St.Dev.	Median	Mean	St.Dev.	Median
IR	695.2	100.5	687.2	269.4	26.8	268.9
LL	1357	2155	666.5	265.7	171.9	247.6
VFA (uncorrected)	1100	151	1102	210.0	65.3	209.5
VFA (corrected)	735.8	96.6	732.7	199.8	55.6	197.0

For muscle tissue, the values of T<sub>1</sub> estimated by the proposed method did not differ significantly from IR ( $p = 0.77$ ), while the uncorrected VFA did differ significantly from IR ( $p = 0.026$ ). For fat tissue, none of the values of T<sub>1</sub> differ significantly from each other. A minor decrease of T<sub>1</sub> can be observed between IR and corrected VFA methods, however, this decrease is not significant ( $p = 0.26$ ).

### 3.3.4 In vivo B<sub>1</sub>-inhomogeneity maps

The initial  $\zeta$ -map computed in the first volunteer study is shown in Figure 3.8a. The corresponding binary weights for the polynomial regression are shown in figure 8b. Most of the discarded points (black in Figure 3.8) were rejected based on the geometric distance criterion (see above), i.e., considered to emanate from noise on the LL data. The black spot at the bottom left emanates from sheer signal loss. The B<sub>1</sub>-inhomogeneity map obtained using weighted polynomial regression is shown in Figure 3.8c. In the fitted B<sub>1</sub>-inhomogeneity map, the inhomogeneous nature of the B<sub>1</sub> field becomes clear: the value for  $\zeta$  in the center has a value of 105%, while it decreases to 70% near the top and bottom following a bell-shaped profile.

For the second volunteer study, the initial  $\zeta$ -map, the binary weights, and the fitted  $\zeta$ -map are shown in Figure 3.9. As before, the location dependency of the B<sub>1</sub>-field is visible. However, in this case, an increase in field strength is observed, with the value for  $\zeta$  reaching 130% near the center. This is also reflected in the uncorrected VFA T<sub>1</sub>-map (Figure 3.7c): the T<sub>1</sub>-values in muscle tissue are higher than expected.

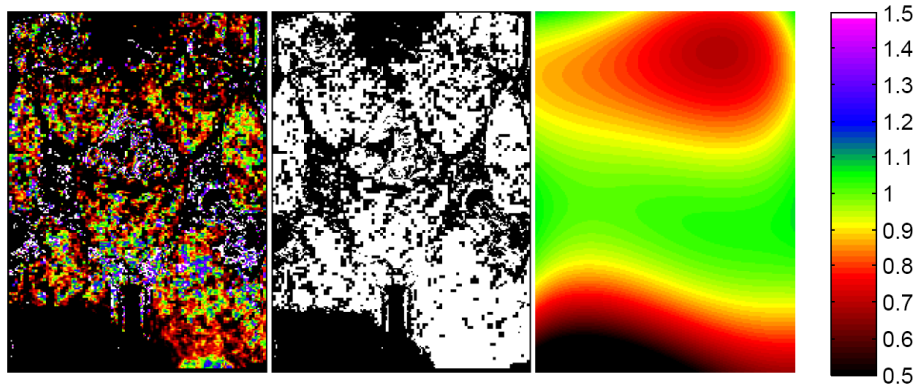


Figure 3.8: (a)  $B_1$ -inhomogeneity map of a human male pelvis. (b) Binary weight map used for fitting (black = 0, white = 1). (c) Fitted  $B_1$ -inhomogeneity map. FOV:  $450 \times 450$  mm<sup>2</sup>.

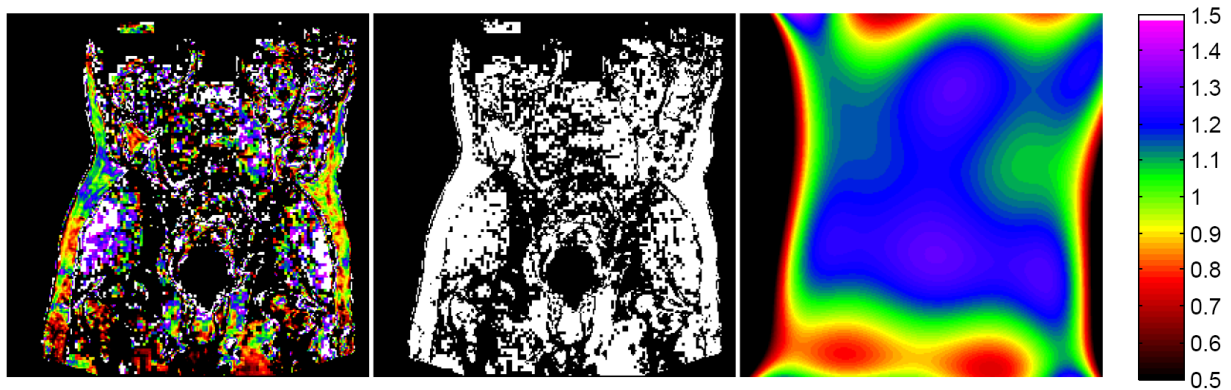


Figure 3.9: (a)  $B_1$ -inhomogeneity map of a human male upper abdomen. (b) Binary weight map used for fitting (black = 0, white = 1). (c) Fitted  $B_1$ -inhomogeneity map. FOV:  $450 \times 450$  mm<sup>2</sup>.

## 3.4 Discussion

### 3.4.1 In vitro experiments

Comparing the four methods' estimated  $T_1$ -values inside the vials, one observes that the corrected VFA method yields a smaller systematic error than both the LL and the uncorrected VFA, while maintaining an acceptable variance level. The difference between the  $T_1$ -values of the corrected VFA technique and IR was not significant ( $p = 0.099$ ), whereas the pooled variance of the corrected VFA technique was significantly lower than the pooled variance of the LL approach ( $p = 0.0001$ ). As such, the  $B_1$ -inhomogeneity map corrected for the attenuation in the applied flip angles.

The averages of the estimated values for  $T_1$  inside the vials obtained with the Look-Locker method and those obtained from the gold standard (IR) were not significantly different ( $p = 0.22$ ). The significantly higher variance of the estimated LL  $T_1$ -values ( $p < 0.0001$ ) was expected, because of its lower SNR. This is a result of the short acquisition time per volume, which is required to keep the total scanning time within one breath-hold.

The  $B_1$ -inhomogeneity map shows a smooth field near the vials, while it diverges towards the edges. The consequence of this effect can also be seen near the edges in the corrected  $T_1$ -map. This divergence is a direct result of the weights used for the polynomial fit: there are no reliable data points in the surrounding water that can guide the polynomial, so the values for  $\zeta$  are solely based on extrapolation. Clearly, this behaviour does not affect the correction inside the ROIs.

### **3.4.2 In vivo experiments**

An insignificant difference between corrected VFA and IR measurements of  $T_1$  was observed in the first in vivo experiment ( $p = 0.084$ ), and likewise in the second in vivo experiment for fat tissue ( $p = 0.26$ ) and for muscle tissue ( $p = 0.77$ ). As such, both the systematic error and the bell-shaped profile were removed in the corrected VFA  $T_1$ -maps. What is more, for the first volunteer study, the pooled variance of the corrected VFA  $T_1$ -map was significantly lower than the pooled variance of the LL  $T_1$ -map ( $p = 0.0006$ ).

Furthermore, the results of both in vivo studies show an increase of  $T_1$  from LL compared to IR, which is caused by outliers in  $T_1$  emanating from the noise on the raw LL data. However, the median  $T_1$  from LL appears to remain unchanged. The LL  $T_1$ -map is used in the calculation of the  $B_1$ -inhomogeneity map, and since outliers in  $T_1$  are likely to cause outliers in  $\zeta$ , these points will be rejected. This makes that the corrected VFA map accurately corresponds to the IR  $T_1$ -map, despite the significant difference between the  $T_1$  values of LL and IR.

In both in vivo studies, a bell-shaped profile from top to bottom (indicated by the arrows in Figure 3.5c) can be observed when comparing the uncorrected VFA  $T_1$ -

maps with IR. This bell-shaped profile was not visible in the in vitro results, which may be due to the compactly clustered arrangement of the vials in the center of the field of view, or due to the reduced generation of standing electromagnetic waves inside the phantom as a result of the rf-pulses (17). Observe that the bell-shaped profiles were removed in the corrected VFA T<sub>1</sub>-maps.

### **3.4.3 Limitations**

A limitation of our work is that the scanning parameters used in the LL and VFA scans were optimized for the range of T<sub>1</sub> values that is expected to occur in our application: from approximately 100 to 1000 ms (at 1.5T). For the LL scans, the timing of the small flip angle pulses was chosen such that the theoretical zero-crossing of the signal would occur during acquisition, whereas for the VFA scans, the range of flip angles was chosen such that the expected Ernst angle would fall within this range. If a local T<sub>1</sub>-value falls outside this range, which is the case for free water, fitting the data fails, resulting in an erroneous T<sub>1</sub> estimate. This effect can be seen in the water surrounding the vials in the phantom scan, but is not an issue for our application.

Second, our method works under the assumption that the B<sub>1</sub>-field is smoothly varying. If this is not the case, for example when the magnetic susceptibility changes rapidly, the smoothing inherent to a low order polynomial fit will result in a B<sub>1</sub>-inhomogeneity map that does not account for this behaviour. This means that in these regions, the T<sub>1</sub>-value will be incorrect. This effect can be mitigated by tuning the order of the polynomial fit: higher orders will allow more rapid changes, but may also cause tissue dependent behaviour, fitting to noise artifacts, and erroneous interpolation or extrapolation. Practically, we have found that a 4<sup>th</sup> or 6<sup>th</sup> order polynomial matched well in several subjects.

Last, we did not explicitly assess the accuracy of the B<sub>1</sub>-inhomogeneity map ( $\zeta$ ). However, the value of  $\zeta$  determines the value of T<sub>1</sub> produced by the corrected VFA method in a one-to-one relation. This one-to-one property results from the fact that the value of  $\zeta$  uniquely defines the apparent Ernst angle. In turn, the apparent Ernst angle is uniquely associated with the value of T<sub>1</sub>. Therefore, the fact that the

differences between the T<sub>1</sub>-values obtained by IR (gold standard) and the corrected VFA are insignificant indicates that the correct value of  $\zeta$  has been obtained.

### **3.5 Conclusion**

We proposed a fast method for estimation and correction of the B<sub>1</sub>-inhomogeneity in FSPGR sequences that requires only two relatively short MRI scans. The data from the two scans (LL and VFA) is combined to produce a T<sub>1</sub>-map of comparable quality as a T<sub>1</sub>-map obtained using the conventional VFA method, while correcting for possible attenuation of the B<sub>1</sub>-field. In addition, the B<sub>1</sub>-attenuation itself is estimated, which can be used to correct the flip angle of other scans based on the FSPGR sequence (e.g., a DCE-MRI scan). Essentially, the proposed method combines the best of two worlds: the high resolution of the VFA method, and the B<sub>1</sub> stability of the LL technique.

### **3.6 Acknowledgements**

Fruitful discussions regarding the fitting procedures with Dirk Poot are greatly appreciated. The research leading to these results was funded from the European Union's Seventh Framework Programme (FP7/2007-2013): the VIGOR++ Project (grant agreement nr. 270379).

### **3.7 References**

1. Verstraete KL, Lang P. Bone and soft tissue tumors: the role of contrast agents for MR imaging. *European journal of radiology* 2000;34(3):229-246.
2. Poncelet E, Delpierre C, Kerdraon O, Lucot JP, Collinet P, Bazot M. Value of dynamic contrast-enhanced MRI for tissue characterization of ovarian teratomas: correlation with histopathology. *Clinical radiology* 2013;68(9):909-916.



3. Hambrock T, Somford DM, Hoeks C, Bouwense SA, Huisman H, Yakar D, van Oort IM, Witjes JA, Futterer JJ, Barentsz JO. Magnetic resonance imaging guided prostate biopsy in men with repeat negative biopsies and increased prostate specific antigen. *The Journal of urology* 2010;183(2):520-527.
4. Chikui T, Kitamoto E, Kawano S, Sugiura T, Obara M, Simonetti AW, Hatakenaka M, Matsuo Y, Koga S, Ohga M, Nakamura K, Yoshiura K. Pharmacokinetic analysis based on dynamic contrast-enhanced MRI for evaluating tumor response to preoperative therapy for oral cancer. *Journal of magnetic resonance imaging : JMRI* 2012;36(3):589-597.
5. Haider MA, Chung P, Sweet J, Toi A, Jhaveri K, Menard C, Warde P, Trachtenberg J, Lockwood G, Milosevic M. Dynamic contrast-enhanced magnetic resonance imaging for localization of recurrent prostate cancer after external beam radiotherapy. *International journal of radiation oncology, biology, physics* 2008;70(2):425-430.
6. Schabel MC, Parker DL. Uncertainty and bias in contrast concentration measurements using spoiled gradient echo pulse sequences. *Physics in medicine and biology* 2008;53(9):2345-2373.
7. Bydder GM, Steiner RE, Young IR, Hall AS, Thomas DJ, Marshall J, Pallis CA, Legg NJ. Clinical NMR imaging of the brain: 140 cases. *AJR American journal of roentgenology* 1982;139(2):215-236.
8. Look DC, Locker DR. Time Saving in Measurement of NMR and EPR Relaxation Times. *Rev Sci Instrum* 1970;41(2):250-251.
9. Shin W, Gu H, Yang Y. Fast high-resolution T1 mapping using inversion-recovery Look-Locker echo-planar imaging at steady state: optimization for accuracy and reliability. *Magnetic resonance in medicine* 2009;61(4):899-906.
10. Fram EK, Herfkens RJ, Johnson GA, Glover GH, Karis JP, Shimakawa A, Perkins TG, Pelc NJ. Rapid calculation of T1 using variable flip angle gradient refocused imaging. *Magnetic resonance imaging* 1987;5(3):201-208.
11. Dowell NG, Tofts PS. Fast, accurate, and precise mapping of the RF field in vivo using the 180 degrees signal null. *Magnetic resonance in medicine* 2007;58(3):622-630.

12. Cunningham CH, Pauly JM, Nayak KS. Saturated double-angle method for rapid  $B_1+$  mapping. *Magnetic resonance in medicine* 2006;55(6):1326-1333.
13. Yarnykh VL. Actual flip-angle imaging in the pulsed steady state: a method for rapid three-dimensional mapping of the transmitted radiofrequency field. *Magnetic resonance in medicine* 2007;57(1):192-200.
14. Nehrke K, Bornert P. DREAM--a novel approach for robust, ultrafast, multislice  $B(1)$  mapping. *Magnetic resonance in medicine* 2012;68(5):1517-1526.
15. Heinrich MP, Jenkinson M, Bhushan M, Martin T, Gleeson FV, Brady SM, Schnabel JA. MIND: modality independent neighbourhood descriptor for multi-modal deformable registration. *Medical image analysis* 2012;16(7):1423-1435.
16. Smit H, Guridi RP, Guenoun J, Poot DH, Doeswijk GN, Milanesi M, Bernsen MR, Krestin GP, Klein S, Kotek G. T1 mapping in the rat myocardium at 7 tesla using a modified CINE inversion recovery sequence. *Journal of magnetic resonance imaging : JMRI* 2014;39(4):901-910.
17. Schick F. Whole-body MRI at high field: technical limits and clinical potential. *European radiology* 2005;15(5):946-959.



# 4 Estimating the AIF from DCE-MRI Data with Compensation for Flow Enhancement (I): Theory, Method and Phantom Experiments

---

## *Abstract*

**Purpose:** To develop a novel method for estimating the Arterial Input Function (AIF) from Dynamic Contrast Enhanced (DCE-) MRI data, while compensating for flow enhancement.

**Materials and Methods:** The proposed method first estimates the number of pulses that spins have received since entering the field of view, and then uses this knowledge to accurately estimate the contrast agent (CA) concentration. The number of pulses is estimated while assuming that the AIF's profile follows Orton's AIF model. The method is evaluated by means of simulations and a phantom experiment.

**Results:** In the simulations, we found that the method can accurately estimate the number of pulses  $n$  (no significant difference between estimated and true  $n$  ( $p = 0.65$ )). Furthermore, the method accurately estimated concentrations  $C$  for a relevant range of number of pulses and concentrations (no significant difference between true and estimated  $C$  for  $40 \leq n \leq 220$  and  $0 \leq C \leq 8$  mmol/L, ( $p > 0.28$ )). The phantom experiment demonstrated that spins in transient state produce the signal intensity expected by the model.

**Conclusion:** The proposed approach accurately corrects the MRI signal affected by the inflow effect.

*To be submitted to: Journal of Magnetic Resonance Imaging*

*Authors: JJN van Schie, C Lavini, LJ van Vliet, FM Vos.*

## **4.1 Introduction**

The Arterial Input Function (AIF) represents the time-dependent arterial contrast agent (CA) concentration, that is used in pharmacokinetic (PK) modelling of dynamic imaging data. Obtaining an accurate AIF is essential for accurate estimation of the PK model parameters. Dynamic Contrast Enhanced MRI often uses a Fast Spoiled Gradient Echo (FSPGR) sequence, for which a theoretic relationship exists between the CA concentration and the signal enhancement assuming that the magnetization resulting from the repeated application of RF-pulses is in a steady state (1,2). Therefore, the AIF is often directly computed from the signal measured in an artery close to the tissue of interest (3).

This assumption does not hold, however, for spins in flowing blood, as they have not spent enough time in the field of view to reach the steady state. Neglecting this can cause a biased estimate of contrast agent concentration, which is detrimental to the estimation of PK parameters (4). The effect manifests itself as a reduction of the signal enhancement, especially at high CA concentrations or for a low number of received pulses. In addition,  $T_2^*$  decay also has a nonlinear effect on the relation between concentration and signal. While this effect can be reduced by choosing a very short echo time, it always causes a bias in the AIF, if not corrected for (5,6).

This is the first of two strongly related articles, in which we focus on the theory, simulations and phantom experiments supporting the proposed methodology for estimating the AIF from DCE-MRI data, in the presence of flow enhancement. The second article deals with automatic procedures applying the new method to patient data and the validation thereof, using clinical data.

### **4.1.1 Related Work**

The AIF can be obtained in several ways. The easiest approach is to use a population-averaged parametrized model (e.g. (7)). Despite its simple implementation, this model ignores inter-subject variations, and is therefore not accurate. It has been shown that the use of a subject-specific AIF improves the robustness of pharmacokinetic analysis (8).

When deriving a subject-specific AIF from the DCE-MRI data, the measured arterial signal needs to be converted to CA concentration. It was proposed that the relation between the concentration and signal intensity could be calibrated with a flow phantom before performing the DCE-MRI scan (9). This produces an unbiased AIF, but needs to be recalibrated for each imaging sequence, and is sensitive to susceptibility differences. It is therefore quite unpractical.

Various authors derive the CA concentration assuming a linear relation between signal intensity and CA concentration (10-12). This is valid for low concentrations and becomes less accurate with higher concentrations, leading to less accurate estimation of PK parameters. Other researchers use the full nonlinear relation between signal intensity and CA concentration, which provides a better estimate of the AIF (13,14), and in turn improves the accuracy of the PK parameter estimates (15). Such nonlinear conversion requires prior knowledge of the  $T_1$  time of blood, which can either be measured in a separate scan, or acquired from literature (16).

Both the linear and the nonlinear conversion methods assume that the measured magnetization is in a steady state, which may not be a valid assumption. The error introduced by this assumption depends on the number of excitation pulses that the spins have received. Although measuring at a downstream location can minimize this effect, this may still be insufficient (17).

#### **4.1.2 Objective**

In this work, we present a novel method to correct the CA concentration measurement in flowing blood. This method takes into account the spin dynamics during the transient state of an FSPGR sequence, including a correction for  $T_2^*$  decay. In order to estimate the AIF, the amount of enhancement due to the inflow effect is estimated first, by constraining the AIF's area under the bolus peak to a fixed value. Subsequently, the estimated amount of enhancement due to flow is compensated as the signal intensity is converted into concentration. We first demonstrate that the method accurately corrects for the inflow effects on computer generated AIFs. Secondly, we test this method in a phantom with a constant flow

velocity and demonstrate that the correction method can accurately estimate the flow velocity.

## 4.2 Materials and Methods

### 4.2.1 Theory

#### FSPGR Magnetization in Transient and Steady State

DCE-MRI is generally performed with a Fast Spoiled Gradient Echo (FSPGR) sequence. This sequence combines a small flip angle excitation of the magnetization with a short repetition time and minimal echo time to obtain images at a high temporal resolution. A spoiler gradient is used to avoid signal contamination by remaining transverse magnetization, thereby achieving  $T_1$ -weighting. The spins' longitudinal magnetization  $M_z$  immediately preceding the  $n+1^{\text{th}}$  excitation can be expressed as a function of the longitudinal magnetization right before the previous excitation  $M_z(n)$ :

$$M_z(n+1) = M_z(n) \cos(\alpha) \exp\left(-\frac{T_R}{T_1}\right) + M_0 \left(1 - \exp\left(-\frac{T_R}{T_1}\right)\right) \quad (4.1)$$

where  $\alpha$  is the applied flip angle,  $T_R$  the repetition time,  $T_1$  the longitudinal relaxation time, and  $M_0$  the net magnetization in equilibrium. Briefly, this equation states that the longitudinal magnetization does not return to the initial state, but instead becomes smaller after each pulse. In the steady state (i.e., after application of a sufficiently large number of RF-pulses),  $M_z(n+1) = M_z(n)$ , and equation (4.1) is commonly rewritten as:

$$M_z = \frac{M_0(1 - E_1)}{1 - \cos(\alpha)E_1} \quad (4.2)$$

with  $E_1 = \exp(-T_R / T_1)$ .

While the spins are in the transient state (i.e., before reaching the steady state), the longitudinal magnetization (expressed recursively in eq. (4.1)) can also be written explicitly in the form of a decaying exponential:

$$M_z(n) = a \exp(b \cdot n) + c \quad \text{with } b < 0 \quad (4.3)$$

Using the boundary condition  $M_z(n=0) = M_0$ , and solving for  $a$ ,  $b$  and  $c$ , gives:

$$a = M_0 \left( 1 - \frac{1 - E_1}{1 - \cos(\alpha) E_1} \right), \quad b = \ln(\cos(\alpha) E_1), \quad c = \frac{M_0(1 - E_1)}{1 - \cos(\alpha) E_1} \quad (4.4)$$

and thus:

$$M_z(n) = M_0 \left( \left( 1 - \frac{1 - E_1}{1 - \cos(\alpha) E_1} \right) (\cos(\alpha) E_1)^n + \frac{1 - E_1}{1 - \cos(\alpha) E_1} \right) \quad (4.5)$$

A detailed derivation of this expression can be found in Appendix A. Note that in the limit where  $n \rightarrow \infty$ , eq. (4.5) reduces to eq. (4.2), i.e., the case of steady state. The MR signal obtained with the FSPGR sequence, measured in the transverse plane after application of an RF-pulse, and taking  $T_2^*$  decay into account, is then:

$$S(n) = \sin(\alpha) M_z(n) \exp(-T_E / T_2^*) \quad (4.6)$$

in which  $T_E$  is the echo time.

In practice, the steady state may not be reached due to flow, in which case not-excited spins entering the field of view perceive an insufficient number of excitations. Consequently, a larger signal can be measured from spins in transient state than from spins in steady state, resulting in *flow enhancement*.

### Signal Intensity Ratio

Gadolinium-based contrast agents enhance the MRI signal by simultaneously reducing the local  $T_1$  and  $T_2^*$  times (2):

$$\begin{aligned} 1/T_1 &= 1/T_{10} + R_1 C \\ 1/T_2^* &= 1/T_{20}^* + R_2^* C \end{aligned} \quad (4.7)$$



in which  $T_{10}$  and  $T_{20}^*$  are the pre-contrast longitudinal and transverse relaxation times respectively,  $R_1$  and  $R_2^*$  are the longitudinal and transverse relaxivities of the contrast agent respectively, and  $C$  is the contrast agent concentration. As such, the longitudinal magnetization  $M_z$  and the measured signal  $S$  become functions of the CA concentration:  $M_z(C, n)$  and  $S(C, n)$ .

The signal ratio  $D$ , defined as the ratio of the post-contrast and pre-contrast MR signal intensities, taking into account the number of excitations ( $n$ ) and  $T_2^*$  decay, for the FSPGR sequence, is given by:

$$D(C, n) = \frac{S(C, n)}{S(0, n)} = \frac{M_z(C, n)}{M_z(0, n)} \exp(-TE r_2^* C) \quad (4.8)$$

Note that in this equation, both  $M_0$  and  $T_{20}^*$  have disappeared. The sequence parameters ( $\alpha$ ,  $TR$  and  $TE$ ), the contrast agent properties ( $r_1$  and  $r_2^*$ ), and the  $T_1$  of blood are (assumed to be) known. However, equation (4.8) is still underdetermined: the concentration  $C$  and the number of pulses  $n$  cannot be determined uniquely without additional information.

### AIF model

To resolve the ambiguity between concentration and the number of pulses, we propose to impose prior knowledge on the CA concentration profile. More specifically, we assume that the profile should follow a slightly modified AIF model described by Orton et al. (18). This model parametrizes the AIF as a sum of two functions, one describing the first passage of the bolus peak, and the other describing wash-out of CA in the tail of the AIF.

The bolus peak  $C_B(t)$  is described by:

$$C_B(t) = a_B \mu_B^2 t \exp(-\mu_B t) u(t) \quad (4.9)$$

with  $u(t)$  the unit step function. The function has been slightly rewritten compared to the one described by Orton et al. (18), such that the area under the curve of  $C_B(t)$  is given by the parameter  $a_B$ , while  $\mu_B$  only affects the decay rate.

The tail of the AIF is expressed as a convolution between the bolus peak and a body transfer function  $G(t)$ , which is modelled as:

$$G(t) = a_G \exp(-\mu_G t) u(t) \quad (4.10)$$

in which  $a_G$  determines the starting level of this decay function and  $\mu_G$  governs the decay rate, which may reflect kidney functioning. Note that if  $\mu_G$  goes to infinity (i.e., the CA is not removed from the blood), the AIF will level off at  $a_B \cdot a_G$ .

Thus, the complete AIF is described as:

$$C_{\text{Orton}}(t, \boldsymbol{\theta}) = C_B(t - t_0) + C_B(t - t_0) * G(t) \quad (4.11)$$

with  $t_0$  a time delay indicating the injection of the bolus and  $\boldsymbol{\theta}$  the vector containing all model parameters:

$$\boldsymbol{\theta} = [a_B, \mu_B, a_G, \mu_G, t_0] \quad (4.12)$$

The shape of the actual AIF may vary per subject, depending on injection rate, concentration of the contrast agent, vascular structure and measurement location. However, the area under the bolus peak of the concentration curve ( $a_B$ , unit: mol·L<sup>-1</sup>·s) is related to the total CA dose (unit: mol) and a subject's average cardiac output (CO, unit: L·s<sup>-1</sup>) by (9):

$$\frac{\text{Dose}}{\text{CO}} = a_B \quad (4.13)$$

Since both the total administered dose and the cardiac output in adults are generally proportional to the subject's body mass (19),  $a_B$  can be expected to be constant among individuals. Hence, we make the assumption that the parameter

$a_B = \frac{a_{B,\text{Orton}}}{\mu_{B,\text{Orton}}^2}$  is identical for each subject, with  $a_{B,\text{Orton}}$  and  $\mu_{B,\text{Orton}}$  as reported by

Orton et al. (18). For a dose per body mass of 0.1 mmol/kg,  $a_B$  is set to:

$$a_B = 50.58 \text{ mmol} \cdot \text{L}^{-1} \cdot \text{s} \quad (4.14)$$

which scales linearly with the dose per body mass.

### Correction Method

When fitting the aforementioned model to arterial data, the free model parameters of equations (4.8) and (4.11) are estimated first by minimizing

$$\hat{\boldsymbol{\theta}}, \hat{n} = \arg \min_{\boldsymbol{\theta}, n} \|D_{\text{meas}}(t) - D(C_{\text{Orton}}(t, \boldsymbol{\theta}), n)\|_2, \quad (4.15)$$

in which  $D_{\text{meas}}$  is a measured signal-ratio curve, and the parameters to be estimated are

$$[\hat{\boldsymbol{\theta}}, \hat{n}] = [\hat{\mu}_B, \hat{a}_G, \hat{\mu}_G, \hat{t}_0, \hat{n}]. \quad (4.16)$$

The parameters are constrained so that they are always positive, and are estimated by means of a nonlinear least squares regression algorithm implemented in Matlab (version R2014b; Mathworks, Natick, USA). In other words, the shape parameters of the modelled concentration curve are adjusted in such a way that the time-ratio curve matches the measured data. Since the area under the bolus peak remains fixed, any discrepancy between the heights of the modelled and measured signal-ratio curves is attributed to flow enhancement, which is accounted for by  $n$ .

Essentially,  $n$  is estimated by comparing an entire time-series of measured data to Orton's model, instead of considering each time-point separately. However, not all information present in the original data is captured in the model (e.g., the presence of a second peak). Therefore, we re-estimate the concentration at each time point using equation (4.8), which is no longer underdetermined after inserting  $\hat{n}$  for the number of pulses the spins have received. This is again done using nonlinear least-squares regression:

$$\hat{C} = \arg \min_C \|D_{\text{meas}} - D(C, \hat{n})\|_2. \quad (4.17)$$

Doing this for every time point in the signal-ratio curve then provides an AIF which takes both flow enhancement and  $T_2^*$  decay into account. Note that in this step, the preliminary estimates for the model parameters  $\hat{\boldsymbol{\theta}}$  are not used.

### Cramér-Rao Analysis

The Cramér-Rao lower bound is the theoretical lower bound on the (co-)variance of any unbiased estimator of parameters. As such, the CRLB matrix can be used to reveal high correlations between model parameters, by computing Pearson's correlation coefficient matrix. Assuming Orton's population-averaged parameters for  $\theta$ ,  $n = 100$  pulses, and not imposing any constraint on  $a_B$ , this correlation coefficient matrix is shown in Figure 4.1a. The high correlations between  $n$  and the other parameters are clearly visible, confirming that these parameters cannot be estimated independently. Alternatively, the proposed constraint on  $a_B$  markedly reduces the correlations between  $n$  and the other parameters (see Figure 4.1b). Essentially, the figure demonstrates that the mere constraint on  $a_B$  allows for precise estimation of  $n$ .

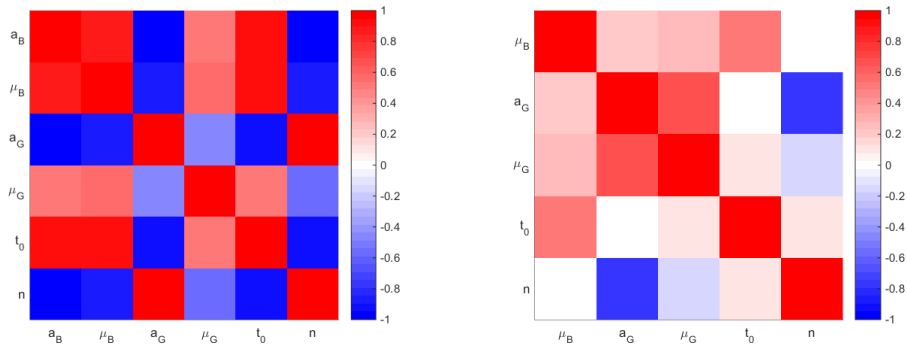


Figure 4.1: Correlation coefficient matrices (a) without; and (b) with imposing a constraint on the  $a_B$  parameter.

### Experimental Design

Two experiments were performed to assess the proposed method's ability to accurately and precisely estimate an AIF from DCE-MRI data. (I) The method was tested on simulated data, in order to quantify its accuracy and precision in estimating the number of pulses (eq. (4.15)), and the CA concentration (eq. (4.17)). (II) The theoretical behaviour of spin dynamics in transient state (eq. (4.6)) was verified in a controlled phantom experiment.

## 4.2.2 Simulation

### Estimating the Number of Pulses

To assess the proposed method's accuracy and precision in estimating the number of pulses  $n$ , it was applied to a simulated set of signal-ratio curves. These signal-ratio curves were created by generating a time-concentration curve (TCC) by means of eq. (4.11), with parameters  $\theta$  describing the population-averaged TCC, as in Orton et al. (18). The TCCs were generated for a duration of 373 seconds and sampled at intervals of 1.247 seconds (300 time points). Next, the TCC was converted into time-intensity curves (TICs) through eq. (4.6). These TICs were generated for different values of  $n$  ranging from 10 to 200 in steps of 10. Thereby, the repetition time and echo time were set to 2.9 and 1.8 ms respectively, the flip angle  $\alpha$  was set to 15 degrees, and the  $T_1$  value of blood was assumed to be 1.779 s (16). The simulated contrast agent was gadobutrol, of which a longitudinal relaxivity  $R_1 = 4.1$  L/mmol/s and a transverse relaxivity  $R_2^* = 6.5$  L/mmol/s was asserted at 3 Tesla (2). All MRI settings were identical to the settings of a patient study, which is described in the adjoined twin paper (REF). Subsequently, Gaussian white noise with an SNR of 20 was added. The TICs were then divided by their average pre-contrast signal to obtain signal-ratio curves. This was repeated 500 times for each value of  $n$ , each time with different noise realizations. Each signal-ratio curve was then processed by the proposed method. See Figure 4.2 for a schematic overview of the simulations. The difference between the median of the estimated values for  $n$  and the true value was considered a measure of the method's accuracy. The interquartile range of the estimated values of  $n$  was taken as a measure of the precision. A two-tailed sign test was applied to determine whether the difference between the medians and each true value was significant, and Fisher's method was used to combine the results into a single  $p$ -value. A  $p$ -value  $< 0.05$  was considered to indicate significance.

### Estimating the Concentration

Similarly, eq. (4.17) was applied to a known set of concentrations to quantify the influence of an error in the estimated value of  $n$  on the subsequently estimated

concentrations. Therefore, a set of concentrations ranging from 0 to 8 mmol/L, in steps of 0.5 mmol/L, was converted to signal ratio by means of eq. (4.8), using a fixed number of pulses  $n$ . The same MRI settings were used as described in the previous subsection. Next, 200 perturbed values  $n_{est}$  were generated around the true  $n$  through the method described in the previous paragraph. Finally, the concentrations were estimated by solving eq. (4.17) for each of the combinations of true concentration and generated  $n_{est}$ . A new set of  $n_{est}$  was generated for each concentration, to ensure statistical independence. This procedure was performed eight times, with  $n$  set to 10, 40, 70, 100, 130, 160, 190 and 220 respectively. Also see Figure 4.2 for an overview of the simulation. The error in the estimated concentrations was assessed in the same manner as indicated in the previous paragraph.

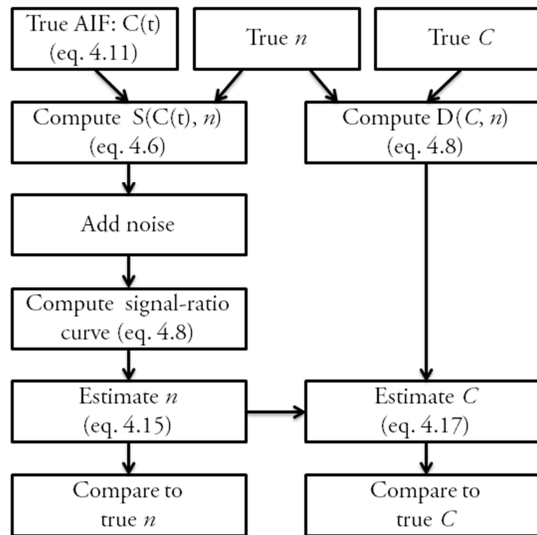


Figure 4.2: Flowchart of the simulations. The left column describes the procedure to estimate the number of pulses  $n$ , while the right column describes the procedure to estimate the concentration  $C$ .

### 4.2.3 Phantom experiment

In order to test the validity of the model describing the signal generated by spins in transient state, i.e., eq. (4.6), a phantom experiment was performed. A liquid was passed through a straight tube, at constant flow velocity  $v$ , while being scanned. This should ensure a linear relation between the distance along the tube  $d$  and the

number of pulses perceived by the spins:  $n = d / (v \cdot TR)$ . The velocity could be estimated by substituting this expression into eq. (4.6) and fitting it to the signal values measured along the tube. Validation of the model was achieved by comparison of the estimated velocity to a reference measurement.

Specifically, the phantom consisted of a flexible plastic tube (4 mm inner diameter) passing through two small, rigid braces of PVC (each 300 mm long), forming a U-tube. The PVC braces were mounted onto the lid of a larger PVC pipe (125 mm inner diameter), with the flexible plastic tube ends extending through the lid. The remaining space inside the larger PVC pipe was filled with agar gel doped with copper sulphate (20g/kg agar powder, 2 mmol/L  $\text{CuSO}_4$ ) to reduce discontinuities in magnetic susceptibility, essentially mimicking tissue surrounding a blood vessel. See Figure 4.3.

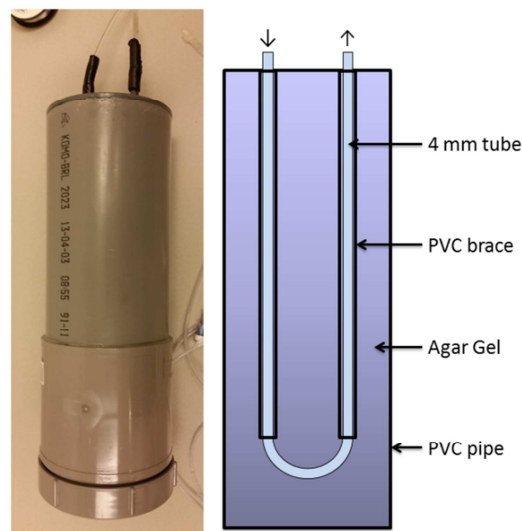


Figure 4.3, Left: Photograph of the flow phantom. Right: Schematic overview of the internal structure of the flow phantom (top view). The arrows at the top indicate flow direction.

A fluid was created by adding copper sulphate to a 0.9% saline solution (1 mmol/L  $\text{CuSO}_4$ ). Despite the differences in viscosity between blood and water, the plastic tube's small inner diameter was expected to ensure laminar flow with a Reynolds number similar to that of blood flowing through the abdominal aorta. An empty IV-bag was filled with 500 ml of this fluid.

First, the IV-bag was scanned with an Inversion Recovery (IR) sequence, allowing to determine the  $T_1$  value of the fluid ( $T_1 = 50, 100, 300, 1000, 1500$  ms,  $T_R = 7000$  ms,  $T_E = 5.3$  ms,  $FOV = 167 \times 167 \times 25$  mm<sup>3</sup>, matrix size =  $336 \times 336 \times 10$  voxels). This  $T_1$  value is required to reliably estimate the velocity by fitting equation (4.6) to the tubes' signal profiles. The  $T_1$ -value of the fluid was determined by fitting the theoretical relationship between the IR signal intensity and  $T_1$  to the measured IR data, using a nonlinear least-squares regression algorithm implemented in Matlab (version R2014b; Mathworks, Natick, USA).

Subsequently, the IV-bag was connected to the inlet tube of the phantom, and suspended 1.20 m above the outlet tube. The tubes inside the phantom were filled with fluid, and the flow was stopped. The phantom was then scanned with a dynamic FSPGR sequence ( $\alpha = 15$  degrees;  $T_R = 2.9$  ms;  $T_E = 1.8$  ms;  $FOV = 200 \times 200 \times 75$  mm<sup>3</sup>; matrix size =  $128 \times 128 \times 30$  voxels; scan time = 250 s; 100 time points). The phantom was scanned axially, so that the tubes were positioned along the slice's phase encoding direction. This was done to ensure that no spins outside the field of view would be excited. After approximately 30 seconds of scanning the stationary fluid, the flow restriction was removed and the fluid was allowed to flow freely under the influence of gravity. During this period, the discharge of fluid was measured using a stopwatch and a graduated beaker, providing a reference estimate of the average flow velocity in the tubes.

The left and right segments of the U-tube were manually segmented from the dynamic series, by selecting two points on the centreline towards the ends of both segments. Subsequently, all voxels with a radial distance smaller than 2 mm to the lines between the points were taken to represent the tube content, and the distance  $d$  of the included voxels along the tube was computed. The intensity profile along the tubes was extracted for three different time intervals: before flow, during flow, and after flow. Then, the theoretical signal relation for spins in transient state (eq. (4.6), substituting  $n = d / (v \cdot TR)$ ) was fitted to each of these profiles. One minor change was made to this signal relation, in that the behaviour of spins outside the field of view was also included in the model. This was done by assuming that a single additional flip angle pulse  $\alpha_{pre}$  preceded the sequence. This would account for



any partial saturation the spins may have before entering the field of view. Particularly, the initial condition used for deriving eq. (4.5) was changed to  $M_z(n=0) = M_0 \cos(\alpha_{pre})$ , resulting in:

$$a = M_0 \left( \cos(\alpha_{pre}) - \frac{1 - E_1}{1 - \cos(\alpha) E_1} \right). \quad (4.18)$$

The inclusion of this effective pre-pulse should only be necessary for the second (right) tube segment, where the spins' longitudinal magnetization may not have relaxed back to equilibrium after being excited in the first (left) tube segment. After the effective pre-pulse, the spins flow through the field of view with velocity  $v$ , producing exponentially decaying signal intensity along the tube. Fitting the model to the signal measured in both tube segments gave an estimate for  $v$  (as well as  $M_0$  and  $\alpha_{pre}$ ). This estimate was compared to the reference velocity.

## 4.3 Results

### 4.3.1 Simulation Results

The results of the Monte Carlo simulations estimating the number of pulses  $n$  by means of eq. (4.15) is shown in Figure 4.4a. Furthermore, the outcome of the experiments estimating the concentrations through eq. (4.17), for five settings of  $n$ , is shown in Figure 4.4b-i. For reference, the estimated concentration assuming  $n = \infty$  is also shown in Figure 4.4b-i.

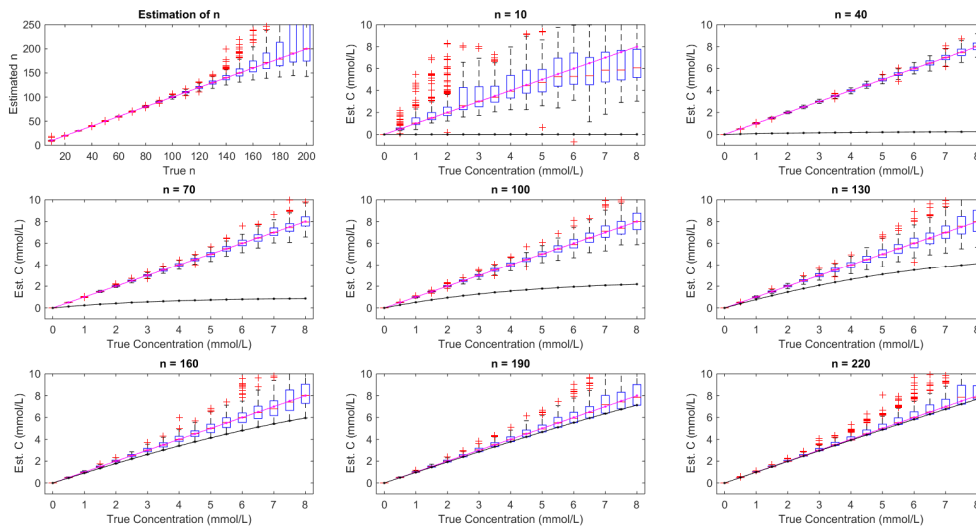


Figure 4.4: Simulation results. (a) Estimated number of pulses  $n$  for true  $n$  ranging from 10 to 200. (b-i) Estimated concentrations for true  $C$  ranging from 0 to 8 mmol/L, for  $n = 10$  to 220 in steps of 30, respectively. In all plots, boxes indicate 25/50/75th percentile, whiskers extend to 1.5 times the interquartile range, red crosses show outliers. The magenta line indicates unity. The black line shows the estimated concentration when assuming  $n = \infty$ .

The medians of the estimated number of pulses were not significantly different from the true values, assessed using Fisher's method ( $p = 0.65$ ). Also, the medians of the estimated concentrations were not significantly different from the true values ( $p = <0.001, 0.28, 0.92, 0.82, 0.91, 0.97, 0.35, 0.60$  for  $n = 10, 40, 70, 100, 130, 160, 190, 220$  respectively). Furthermore, it is clearly visible that estimating the concentration while wrongfully assuming  $n = \infty$  results in a significant underestimation of the concentration, especially at lower values of  $n$  and at higher concentrations.

The interquartile ranges of the estimations of the concentrations are plotted separately in Figure 4.5. Clearly, the estimation uncertainty increases when the true concentration increases, though the relation between the uncertainty and the number of pulses is more complicated.

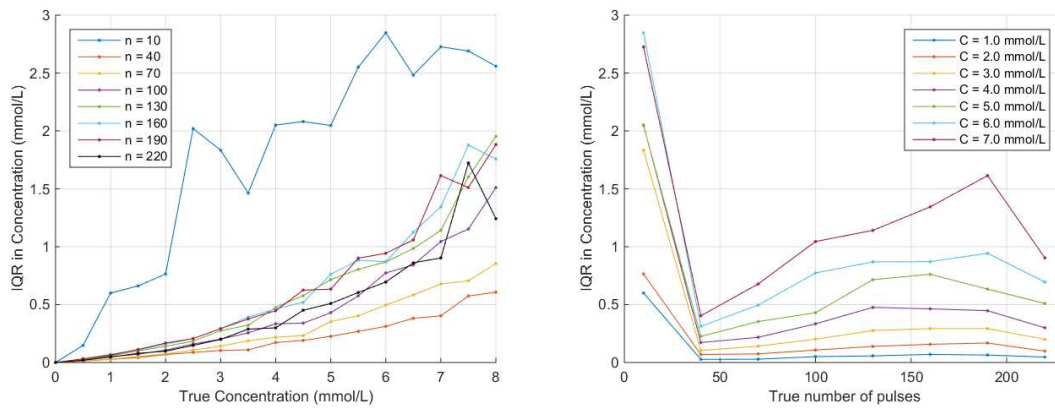


Figure 4.5: Interquartile ranges in estimated concentrations, (a) for different number of pulses  $n$ , (b) for different concentrations.

### 4.3.2 Phantom Experiment Results

The average velocity of the fluid passing through the phantom, as measured with a graduated beaker and stopwatch, was found to be 21 cm / s.

The  $T_1$ -value of the fluid, estimated in a manually selected region of interest in a  $T_1$ -map produced using an Inversion recovery sequence, was 1071.8 +/- 9.4 ms.

False coloured images acquired with the dynamic FSPGR sequence before, during and after flow are shown in Figure 4.6. The enhanced signal intensity due to flow is clearly visible in the middle row, especially in the left tube segment. The intensity profiles along the tube segments for each time interval are shown in Figure 4.7. The decaying exponential behaviour of the signal during flow (cf. eq. (4.6)) is clearly visible. Additionally, the signal shows marked enhancement on the inflow sides of the tubes. Reversely, there is a reduced signal intensity further downstream (compared to the stationary case), which we attribute to the mixing of spins with different velocities. These spins will have different phase encodings within a voxel, and therefore slightly cancel each other out. Furthermore, the signal intensity on the inflow side in the right tube is lower than on the inflow side of the left tube, because the spins have not fully relaxed to equilibrium after being excited in the left tube.

Figure 4.7 also shows the result of fitting the theoretical model for the physical behaviour of the spins (eq. (4.6)) to the measured data. For the left tube, the estimated velocity was 191.5 mm/s, while the effective pre-pulse was negligibly small. For the right tube, the estimated velocity was 189.9 mm/s, and the effective pre-pulse 10.64 degrees. Observe that both estimated velocities are within 10% of the reference value.

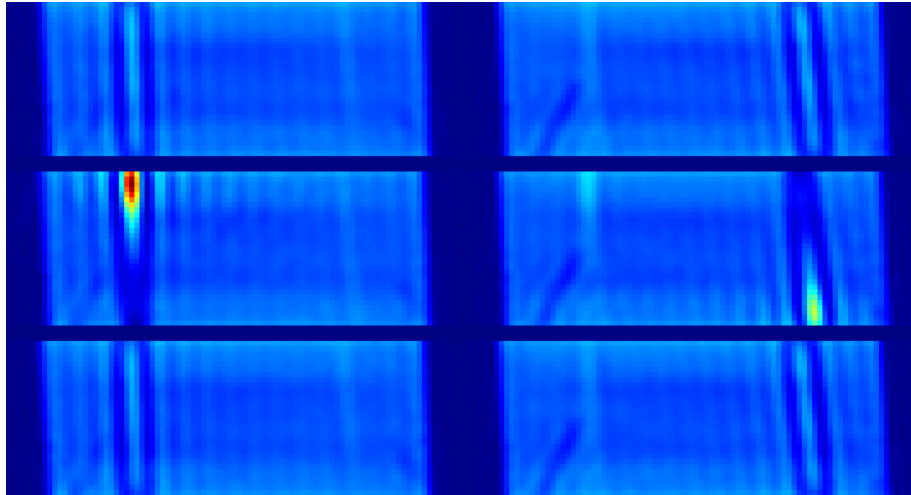


Figure 4.6: Acquisitions of the phantom before flow (top row), during flow (middle row) and after flow (bottom row), at two slice positions through the phantom. Fluid flows downwards in the left tube (middle left) and upwards in the right tube (middle right), showing the inflow effect.

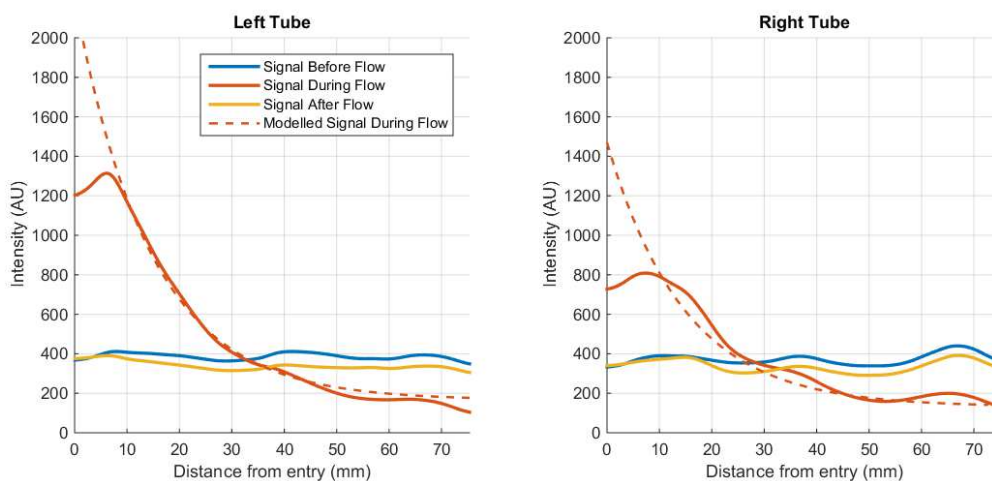


Figure 4.7: Solid lines: intensity profiles along both tube segments, for time intervals before, during and after flow. Dashed lines: theoretical model fitted to the measured signal during flow.

## **4.4 Discussion**

The results presented in the previous section show that our flow correction method is accurate (i.e., able to reproduce the true number of pulses and concentration) and precise (i.e., robust in the presence of noise) when applied to the phantom and simulated data.

### **4.4.1 Simulation**

The Monte Carlo simulations with varying number of pulses  $n$  (Figure 4.4a) show that the estimates of  $n$  by our method remain unbiased over a wide range of reference values. However, the spread in the estimations increases with larger true  $n$ . This is expected, since increasing the number of pulses brings the MR signal closer to the steady state. This hinders the estimation, as the signal intensity no longer depends on  $n$ .

Similarly, the Monte Carlo simulations for varying CA concentrations demonstrate that our method also yields unbiased concentration estimates (Figure 4.4b-i) in all cases, except for very low  $n$ . The spread in the estimated concentrations increases with increasing  $C$ , due to the MR signal levelling off at higher concentrations. Therefore, the signal intensity no longer relates to the CA concentration, which decreases the precision of the estimates. The spread in the estimated concentration as a function of number of pulses is more complicated. For very low true values of  $n$ , the effect of CA on the MRI signal is very small, so noise has a large effect on the estimation of  $C$ . At medium true values of  $n$  (around 80 pulses), the derivative of the signal ratio w.r.t.  $n$  is large, which translates to a low spread in  $C$ . Then, at higher true values of  $n$  (around 150 pulses), the spread in the estimated values of  $n$ , and thereby the spread in  $C$ , increases. Finally, when the spins reach steady state, the effect of errors in the estimated values of  $n$  have less influence on the estimation of  $C$ , and the spread decreases again.

Thus, the proposed method requires moderate levels of CA (within the physiologically expected range), as is the case with any method for deriving the concentration from the signal intensity. Furthermore, the method is appropriate

when the number of pulses is below the level of steady state. Reversely, wrongly assuming that the spins are always in steady state yields a marked underestimation of the concentration, as demonstrated by the black lines in Figure 4.4b-f. This signifies that the inflow effect should be taken into account when computing the CA concentration

#### **4.4.2 Phantom Experiments**

From the MR acquisitions of the flow phantom (Figure 4.7), it becomes apparent that the inflow of fresh spins into the field of view can have a large effect on the signal intensity. Simultaneously, the measured intensities behave according to the presented theory of spin dynamics in transient state. Particularly, the estimated velocities in the two tube segments are in agreement with each other, as well as with the reference measurement.

#### **4.4.3 Limitations**

A limitation of the proposed method follows from constraining the area under the bolus peak to a fixed value. This might introduce a bias in the estimation of  $n$ , and therefore in the estimation of  $C$ . However, it was reported by Parker et al. that the relative standard error in the model parameter corresponding to the area under the bolus peak is only 5.4% (7). This suggests that there is indeed little deviation in  $a_B$  among people.

Another limitation of the method is that noise on the MR signal can introduce errors in the estimation of  $C$ . It is therefore beneficial if the method is applied to the signal from several voxels simultaneously, so that a median AIF can be computed. Clearly, this may require alignment of the data.

Finally, the MR signal becomes a function not only of the number of pulses, but also of the amplitude of the perceived excitation pulse, in the case that the exciting  $B_1$ -field is inhomogeneous. This effect can be included easily in the proposed model, if the  $B_1$ -field is calibrated.

## 4.5 Conclusion

We have presented a method to estimate and correct for flow enhancement that can affect the estimation of the AIF. The simulations show that the proposed method (1) sustains accurate estimation of the perceived number of pulses by flowing spins; (2) uses this information to accurately quantify the concentration of contrast agent. Furthermore, the flow phantom experiment demonstrates that spins in transient state indeed produce the expected signal intensity: decaying exponentially with increased number of pulses. It confirms that the proposed approach is fully in agreement with the theory.

## 4.6 Acknowledgements

We would like to express our gratitude to Ron Hoogerheide for the construction of the flow phantom. The research presented in this paper was funded from the European Union's Seventh Framework Programme (FP7/2007-2013): the VIGOR++ Project (grant agreement nr. 270379).

## 4.7 Appendix

### 4.7.1 Appendix A: Derivation of the Formula for $M_z$ in Explicit Form

The recursive expression for  $M_z$  follows from the Bloch equations for an FSPGR sequence:

$$M_z(n+1) = M_z(n)\cos(\alpha)E_1 + M_0(1 - E_1). \quad (4.19)$$

To make this expression explicit, we try a generic decaying exponential with offset:

$$M_z(n) = a \cdot \exp(b \cdot n) + c \quad (4.20)$$

for some parameters  $a$ ,  $b < 0$ , and  $c$ . Substituting  $n+1$  for  $n$  in eq. (4.20), and rearranging the terms, gives:

$$M_z(n+1) = (a \cdot \exp(b \cdot n) + c - c) \exp(b) + c. \quad (4.21)$$

Now  $M_z(n)$  (eq. (4.20)) can be substituted in the right-hand side of eq. (4.21). After substitution and more rearrangement of terms, we get:

$$M_z(n+1) = M_z(n) \exp(b) + c(1 - \exp(b)). \quad (4.22)$$

Equating the right-hand sides of eq. (4.19) and eq. (4.22), and solving for  $b$  and  $c$ , gives:

$$b = \ln(\cos(\alpha) E_1) \quad \text{and} \quad c = \frac{M_0(1 - E_1)}{1 - \cos(\alpha) E_1}. \quad (4.23)$$

Then, substituting the boundary condition  $M_z(n=0) = M_0$  to eq. (4.20), and solving for  $a$ , gives:

$$a = M_0 \left( 1 - \frac{1 - E_1}{1 - \cos(\alpha) E_1} \right). \quad (4.24)$$

Finally, combining equations (4.20), (4.23) and (4.24) gives:

$$M_z(n) = M_0 \left( \left( 1 - \frac{1 - E_1}{1 - \cos(\alpha) E_1} \right) (\cos(\alpha) E_1)^n + \frac{1 - E_1}{1 - \cos(\alpha) E_1} \right) \quad (4.25)$$

Note that the assumption  $b < 0$  only holds if  $0 < \cos(\alpha) E_1 < 1$ . The latter inequality always holds, but the former may be violated for flip angles larger than 90 degrees. In this case  $M_z$  cannot be described by a decaying exponential function.

## 4.8 References

1. Fram EK, Herfkens RJ, Johnson GA, Glover GH, Karis JP, Shimakawa A, Perkins TG, Pelc NJ. Rapid calculation of T1 using variable flip angle gradient refocused imaging. *Magnetic resonance imaging* 1987;5(3):201-208.



2. Stalder AF, von Elverfeldt D, Paul D, Hennig J, Markl M. Variable echo time imaging: Signal characteristics of 1-M gadobutrol contrast agent at 1.5 and 3T. *Magnetic Resonance in Medicine* 2008;59(1):113-123.
3. Schabel MC, Parker DL. Uncertainty and bias in contrast concentration measurements using spoiled gradient echo pulse sequences. *Physics in medicine and biology* 2008;53(9):2345-2373.
4. Roberts C, Little R, Watson Y, Zhao S, Buckley DL, Parker GJ. The effect of blood inflow and B(1)-field inhomogeneity on measurement of the arterial input function in axial 3D spoiled gradient echo dynamic contrast-enhanced MRI. *Magnetic resonance in medicine : official journal of the Society of Magnetic Resonance in Medicine / Society of Magnetic Resonance in Medicine* 2011;65(1):108-119.
5. De Naeyer D, Debergh I, De Deene Y, Ceelen WP, Segers P, Verdonck P. First order correction for T2\*-relaxation in determining contrast agent concentration from spoiled gradient echo pulse sequence signal intensity. *Journal of magnetic resonance imaging : JMRI* 2011;34(3):710-715.
6. Wang H, Cao Y. Correction of arterial input function in dynamic contrast-enhanced MRI of the liver. *Journal of magnetic resonance imaging : JMRI* 2012;36(2):411-421.
7. Parker GJ, Roberts C, Macdonald A, Buonaccorsi GA, Cheung S, Buckley DL, Jackson A, Watson Y, Davies K, Jayson GC. Experimentally-derived functional form for a population-averaged high-temporal-resolution arterial input function for dynamic contrast-enhanced MRI. *Magnetic resonance in medicine* 2006;56(5):993-1000.
8. Rijpkema M, Kaanders JH, Joosten FB, van der Kogel AJ, Heerschap A. Method for quantitative mapping of dynamic MRI contrast agent uptake in human tumors. *Journal of magnetic resonance imaging : JMRI* 2001;14(4):457-463.
9. Ivancevic MK, Zimine I, Montet X, Hyacinthe JN, Lazeyras F, Foxall D, Vallee JP. Inflow effect correction in fast gradient-echo perfusion imaging. *Magnet Reson Med* 2003;50(5):885-891.
10. Zollner FG, Zimmer F, Klotz S, Hoeger S, Schad LR. Renal perfusion in acute kidney injury with DCE-MRI: deconvolution analysis versus two-compartment filtration model. *Magnetic resonance imaging* 2014;32(6):781-785.

11. Taouli B, Johnson RS, Hajdu CH, Oei MT, Merad M, Yee H, Rusinek H. Hepatocellular carcinoma: perfusion quantification with dynamic contrast-enhanced MRI. *AJR American journal of roentgenology* 2013;201(4):795-800.
12. Lim SW, Chrysochou C, Buckley DL, Kalra PA, Sourbron SP. Prediction and assessment of responses to renal artery revascularization with dynamic contrast-enhanced magnetic resonance imaging: a pilot study. *American journal of physiology Renal physiology* 2013;305(5):F672-678.
13. Jensen RL, Mumert ML, Gillespie DL, Kinney AY, Schabel MC, Salzman KL. Preoperative dynamic contrast-enhanced MRI correlates with molecular markers of hypoxia and vascularity in specific areas of intratumoral microenvironment and is predictive of patient outcome. *Neuro-oncology* 2014;16(2):280-291.
14. Rajan S, Herbertson L, Bernardo M, Choyke P. A dialyzer-based flow system for validating dynamic contrast enhanced MR image acquisition. *Magnetic resonance in medicine : official journal of the Society of Magnetic Resonance in Medicine / Society of Magnetic Resonance in Medicine* 2014;72(1):41-48.
15. Aronhime S, Calcagno C, Jajamovich GH, Dyvorne HA, Robson P, Dieterich D, Fiel MI, Martel-Laferriere V, Chatterji M, Rusinek H, Taouli B. DCE-MRI of the liver: effect of linear and nonlinear conversions on hepatic perfusion quantification and reproducibility. *Journal of magnetic resonance imaging : JMRI* 2014;40(1):90-98.
16. Shimada K, Nagasaka T, Shidahara M, Machida Y, Tamura H. In vivo Measurement of Longitudinal Relaxation Time of Human Blood by Inversion-recovery Fast Gradient-echo MR Imaging at 3T. *Magn Reson Med Sci* 2012;11(4):265-271.
17. Garpebring A, Wirestam R, Ostlund N, Karlsson M. Effects of inflow and radiofrequency spoiling on the arterial input function in dynamic contrast-enhanced MRI: a combined phantom and simulation study. *Magnetic resonance in medicine* 2011;65(6):1670-1679.
18. Orton MR, d'Arcy JA, Walker-Samuel S, Hawkes DJ, Atkinson D, Collins DJ, Leach MO. Computationally efficient vascular input function models for quantitative kinetic modelling using DCE-MRI. *Physics in medicine and biology* 2008;53(5):1225-1239.

19. deSimone G, Devereux RB, Daniels SR, Mureddu G, Roman MJ, Kimball TR, Greco R, Witt S, Contaldo F. Stroke volume and cardiac output in normotensive children and adults - Assessment of relations with body size and impact of overweight. *Circulation* 1997;95(7):1837-1843.

# 5 Estimating the AIF from DCE-MRI Data with Compensation for Flow Enhancement (II): Applications in Spine Diagnostics and Assessment of Crohn's Disease

---

## *Abstract*

**Purpose:** To evaluate a newly developed method for subject-specific Arterial Input Function (AIF) estimation that takes inflow effects into account.

**Materials and Methods:** The AIFs obtained with the new method were compared to AIFs obtained from distally placed ROIs, as well as to a population-averaged AIF. The AIFs were used with Tofts' extended two-compartment pharmacokinetic (PK) model. The methods were applied to two DCE-MRI patient studies: a study concerning the spine, acquired with a variety of scan settings, and a study concerning Crohn's Disease patients, acquired with identical scan settings. The Crohn's Disease Index of Severity (CDEIS) was determined for the latter group, which was correlated to the estimated  $K_{\text{trans}}$  parameters.

**Results:** Both the medians and the variances in  $v_p$  were significantly larger when using the distal ROI approach, compared to the other methods. Furthermore, the distal ROI method yielded unrealistic parameter estimations in several cases. There were no significant differences between the medians or variances of the  $K_{\text{trans}}$  parameter of the proposed method and the population-average approach. In the Crohn's Disease study, the estimated  $K_{\text{trans}}$  parameter correlated better with the CDEIS when the proposed AIF was used, compared to AIFs from the distal ROI method or the population-averaged AIF.

**Conclusion:** The proposed method yielded realistic PK model parameters while applying a range of scan settings, and improved the correlation of the  $K_{\text{trans}}$  parameter with CDEIS, compared to a population-average AIF.

*To be submitted to: Journal of Magnetic Resonance Imaging*

*Authors: JJN van Schie, C Lavini, LJ van Vliet, FM Vos, G Kramer, I Pieters, JT Marcus, J Stoker*

## 5.1 Introduction

Dynamic Contrast Enhanced MRI (DCE-MRI) is an important radiological technique with a wide range of applications. It is used to study physiological processes involving tissue perfusion in qualitative (1,2) and quantitative (3,4) ways. Several pharmacokinetic (PK) models are available to quantitatively estimate parameters describing microvascular density and integrity (5). An essential component of PK models is the Arterial Input Function (AIF). The AIF represents the time-dependent concentration of contrast agent (CA) in the blood plasma supplied to the tissue of interest. A correct representation of the AIF is essential for accurate estimation of the PK model parameters.

The AIF is usually obtained by either measuring the concentration from the DCE-MRI data directly, or by using a population-averaged, parametrized model from literature (e.g., (6)). When measuring the AIF from the DCE-MRI data, either the full nonlinear relationship between the CA concentration and the MRI signal in an artery close to the tissue of interest is used (7), or a simplified linear approximation is adopted (3,8). Generally speaking, a more accurate AIF leads to a more accurate PK analysis (9,10).

DCE-MRI often uses a Fast Spoiled Gradient Echo (FSPGR) sequence, for which a theoretic relationship exists between the CA concentration and the signal enhancement, under the assumption that the magnetization after the repeated application of RF-pulses is in a steady state (11,12). In the case of flowing spins, such as in arterial blood, the assumption of steady state may not hold, as freshly inflowing spins have not received sufficient RF-pulses to reach steady state. This effect is particularly evident upstream in larger arteries, where it manifests by a diminished enhancement. This inflow effect introduces a significant bias in the estimation of the AIF, if not accounted for (13). The influence of flow may be reduced by estimating the AIF in a region distal from the entry point of an artery into the field of view, yet this may not be sufficient.

This paper is the second of two related papers. In the first paper, we presented a novel method of estimating the AIF from DCE-MRI data, which corrects for signal

enhancement as a result of inflow effects. The objective of the current paper is to evaluate this novel algorithm in vivo, and to verify the necessity of correcting for the inflow effect. We assess the robustness of this technique by applying it to DCE-MRI scans obtained with different scanning protocols. We then use the estimated AIF for pharmacokinetic modelling.

## 5.2 Materials and Methods

### 5.2.1 Theory

The AIF estimation method models the spin dynamics during the transient state of an FSPGR sequence after contrast agent injection. Specifically, an analytic expression was found for the signal ratio  $D$  between post- and pre-contrast signal intensities in an artery as a function of the CA concentration  $C$  and the number of excitation pulses  $n$  perceived by the spins:

$$D(C, n) = \frac{(1 - Q(C))(\cos(\alpha)E_1(C))^n + Q(C)}{(1 - Q(0))(\cos(\alpha)E_1(0))^n + Q(0)} \exp(-T_E R_2^* C) \quad (4.26)$$

With

$$Q(C) = \frac{1 - E_1(C)}{1 - \cos(\alpha)E_1(C)} \quad \text{and} \quad E_1(C) = \exp\left(-T_R \left(\frac{1}{T_{10}} + R_1 C\right)\right) \quad (4.27)$$

Unfortunately, this equation is underdetermined:  $C$  and  $n$  cannot be determined uniquely from a given signal ratio without additional information. In other words, a given MRI signal may be increased due to a higher concentration of contrast agent, or due to a reduced number of pulses.

We solved this ambiguity by assuming that the CA concentration should follow a specific pattern over time. As such, we adopted the second AIF model described by Orton et al. (14). The shape of Orton's AIF model was allowed to vary per subject, e.g., due to varying injection rate, concentration of the contrast agent, vascular structure, excretion rate and measurement location. However, the area under bolus

peak of the concentration curve (AUC) was assumed to be constant among individuals. This is a reasonable assumption, since the AUC can be expressed as the ratio between the dosage of contrast agent and the subject's cardiac output (15), which both scale linearly with body mass (16).

Inserting Orton's parameterized model into the analytic expression for the signal ratio models the signal ratio over time. The number of RF-pulses  $n$  experienced by the flowing spins in a voxel is estimated by fitting the modelled ratio over time to a measured signal-ratio curve. Essentially, the parameters of the modelled concentration curve are adjusted in such a way that the curve matches the measured data. Because the area under the bolus peak is constrained, any discrepancy between the heights of the modelled and measured signal-ratio curves is attributed to flow enhancement, which is accounted for by the number of excitation pulses. In this way, the number of pulses  $n$  can be estimated.

Finally, the CA concentration is re-estimated from the signal-ratio expression at each time point separately, using the previously estimated number of pulses. This step is necessary to ensure that any additional information, which may be present in the original data, but was not included in the modelled concentration profile (e.g. the presence of a recirculation peak), is retained. Since the signal-ratio expression (eq. (4.26)) is no longer underdetermined, the concentration can be determined in the artery as a function of time, and the AIF is obtained.

Further details about the derivation can be found in Chapter 4.

### **5.2.2 Patients**

Two separate datasets were used for evaluation purposes. The first dataset was obtained from 13 clinical patients who were referred for an MRI using contrast agent for variety of spine related complaints. All these patients were consecutively included in the frame of a DCE-MRI protocol optimization study. The second dataset was from 21 consecutive patients from a recently concluded prospective study into luminal Crohn's Disease (publication in preparation). Ileocolonoscopy was performed within two weeks of the MRI scan by a gastroenterologist. The

endoscopist applied the Crohn's Disease Endoscopic Index of Severity (CDEIS) to assess endoscopic disease activity. The local Medical Ethics Committee approved both studies. All patients had given informed consent to usage of their data.

### **5.2.3 MRI Acquisition Protocols**

DCE-MR imaging was performed with FSPGR sequences on two 3.0 Tesla scanners in two different medical centres (VUMC Amsterdam and AMC Amsterdam): Philips Ingenuity for the spine patients and Philips Ingenia for the Crohn's patients (both scanners were from Philips, Best, The Netherlands). Care was taken that the descending aorta was clearly visible in all acquired data.

In the first dataset, the scans were made with a range of settings, to explore the method's ability to obtain an AIF under various conditions. The scan parameters were: sagittal orientation, matrix size:  $256 \times 256 \times [4 - 6]$  voxels, FOV:  $320 \times 320 \times [16.0 - 22.5]$  mm<sup>3</sup>,  $T_R = [3.2 - 4.3]$  ms,  $T_E = [1.4 - 2.7]$  ms,  $\alpha = [10 - 15]$  degrees, with temporal resolutions of  $[4.26 - 7.51]$  s, for a total scan time of  $[213 - 376]$  s ( $[50 - 70]$  volumes). After approximately 30 seconds, a bolus injection of gadoterate meglumine (Dotarem 0.5 mmol/ml; Guerbet; Roissy; France) was administered intravenously, at a rate of 3 ml/s, for a total dose of 0.1 mmol/kg body mass.

In the second dataset, all scans were made with identical settings (coronal orientation, matrix size:  $224 \times 224 \times 20$  voxels, FOV:  $400 \times 400 \times 50$  mm<sup>3</sup>,  $T_R = 2.86$  ms,  $T_E = 1.80$  ms,  $\alpha = 15^\circ$ ) with a temporal resolution of 1.27 s, for a total scan time of 381 seconds (300 volumes). After approximately one minute, a bolus injection of gadobutrol (Gadovist 1.0 mmol/ml; Schering AG, Berlin, Germany) was administered intravenously, at a rate of 5 ml/s, for a total dose of 0.1 mmol/kg body mass.

### **5.2.4 Artery Selection and AIF Estimation**

The first step in estimating the AIF from a DCE-MRI dataset was to segment the aorta and iliac arteries. In the first dataset, the lower temporal resolution and higher degree of noise necessitated a manual segmentation. This was done by selecting



voxels inside manually drawn polygons. In the second dataset, an automatic segmentation method was applied. This automatic segmentation method was based on an empiric approach relying on two properties of the data: the time to peak is relatively short, and there is a marked change in intensity. The segmentation method is described in detail in appendix A.

Next, a signal-ratio curve was computed in each voxel from the segmented region, by dividing the measured signal by the average pre-contrast signal (see appendix A). From each signal-ratio curve, the corresponding number of pulses  $n$  was computed, and, with the number of pulses known, time-concentration curves (TCCs) were computed. (See the theory section above, or section 4.2.1 on page 46.)

After all the TCCs were computed, they were aligned to each other based on the estimated time shift (see appendix A), while using linear interpolation. Since the distribution of the estimated concentrations at a given time point is skewed, the mode of the data at each time point was chosen as the best estimate for the concentration. The mode was computed using a mean-shift procedure with a Gaussian kernel (17). Furthermore, the full width at half the maximum was chosen as the measure of uncertainty. A schematic overview of the entire procedure is shown in Figure 5.1.

The proposed method was compared to an approach in which a TCC was computed from a small, manually drawn ROI in the iliac artery, distal from the entry point of the aorta into the field of view. The concentration was computed from the MRI signal in these ROIs while assuming an infinite number of pulses, as is done traditionally (13). Furthermore, the AIF from the proposed method was compared to the population averaged, parameterized AIF presented by Orton et al. (14).

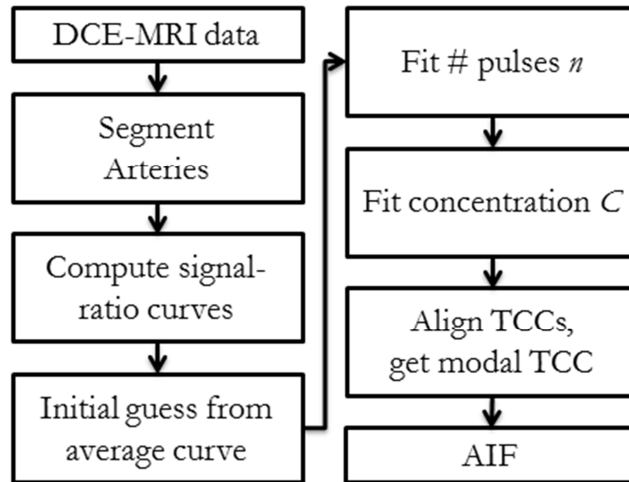


Figure 5.1: Schematic overview of the procedure of estimating the AIF from DCE-MRI data.

### 5.2.5 Pharmacokinetic Analysis

For each DCE-MRI acquisition of the first dataset, a region of interest was manually drawn inside vertebra considered healthy by an experienced radiologist (IP). From these ROIs, TICs were extracted and averaged. These TICs were then converted to TCCs, using the same method as described above, but setting the number of pulses to infinity. This is allowed, since the ROIs were constantly inside the field of view, and the magnetization was therefore in the steady state. The  $T_{10}$  time of the bone tissue was set to 586 ms (18).

For each acquisition of the second dataset, the volumes at each time point were registered to each other using the method of Li et al. (19), to compensate for motion of the tissue. Subsequently, regions presenting active Crohn's Disease were identified by an expert abdominal radiologist (JS). The presence of active Crohn's Disease was based on other available MRI sequences. A research fellow delineated each such region as instructed by the radiologist. TICs were extracted from these ROIs, averaged, and converted to TCCs. In the absence of a literature value for the  $T_{10}$ -time of bowel tissue, the  $T_{10}$ -time was set to 700 ms.

The pharmacokinetic properties of the investigated tissues were determined using Tofts' extended two-compartment PK model (5). Here, the tissue concentration is modelled as a function of the plasma concentration  $C_p = AIF/(1-Hct)$ , as well as

the volume fractions of plasma ( $v_p$ ), interstitial space ( $v_e$ ), and the transfer rate coefficient ( $K_{ep}$ ). These factors were estimated numerically by fitting Tofts' model to the measured time-concentration curve in the tissue, using least-squares regression. The haematocrit value  $Hct$  was set to 0.42. The procedure was performed for the patients of both datasets, with AIFs obtained with the three methods described. The root mean square errors (RMSE) of the fits averaged over all patients were compared to assess the appropriateness of the methods. This was done using the student's t-test. The median values of the pharmacokinetic model parameters obtained with the three methods were compared using a Mann-Whitney U test. The associated variances were statistically assessed by the Brown-Forsythe test. Finally, the volume transfer coefficients  $K_{trans} = v_e \cdot K_{ep}$  were computed for the patients of the second dataset, and compared to the CDEIS score of each patient. Spearman's rank correlation coefficient was computed for each AIF extraction method, as an indirect, quantitative measure of the usefulness of the methods. A value of  $p < 0.05$  was considered statistically significant in all the statistical assessments.

## 5.3 Results

### 5.3.1 Results from the Spine Data

In the dataset of the 13 spine patients, the quality of the arterial signal was very heterogeneous, ranging from TICs with a pronounced peak to others with an almost invisible peak. These acquisitions were processed according to the proposed method (also see Figure 5.1). The estimated number of pulses in each segmented voxel was mapped back into a volume to produce an ' $n$ -map' of each dataset. Maximum intensity projections along the sagittal direction of two representative  $n$ -maps are shown in Figure 5.2. Note that the number of pulses increases from top to bottom, corresponding to the direction of the blood flow.

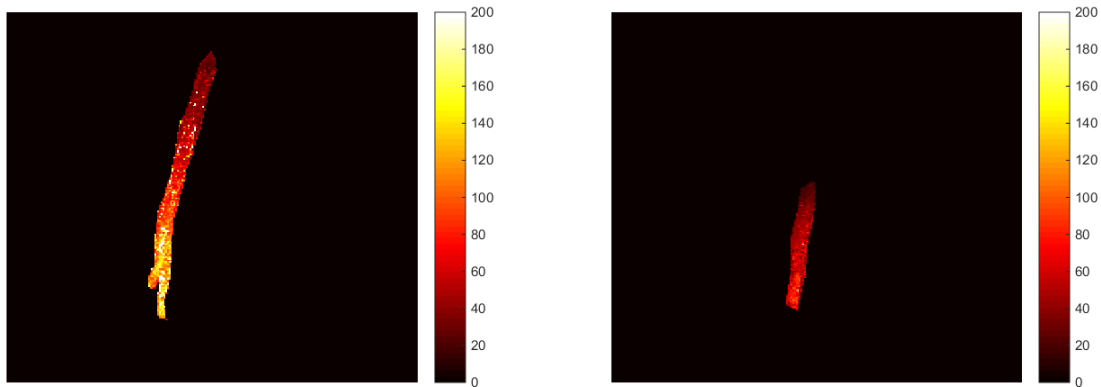


Figure 5.2: Maximum intensity projections of  $n$ -maps in the sagittal direction of two subjects from the spine study. The arteries were segmented manually.

Two representative modal AIFs, estimated using the two  $n$ -maps of Figure 5.2, are shown in Figure 5.3. Also, the AIFs estimated using the ROI method (assuming infinite pulses), as well as Orton's population-averaged AIF is shown in the same graphs. Notice that the proposed method can correct for the almost completely absent initial peak in the original AIFs (magenta lines).

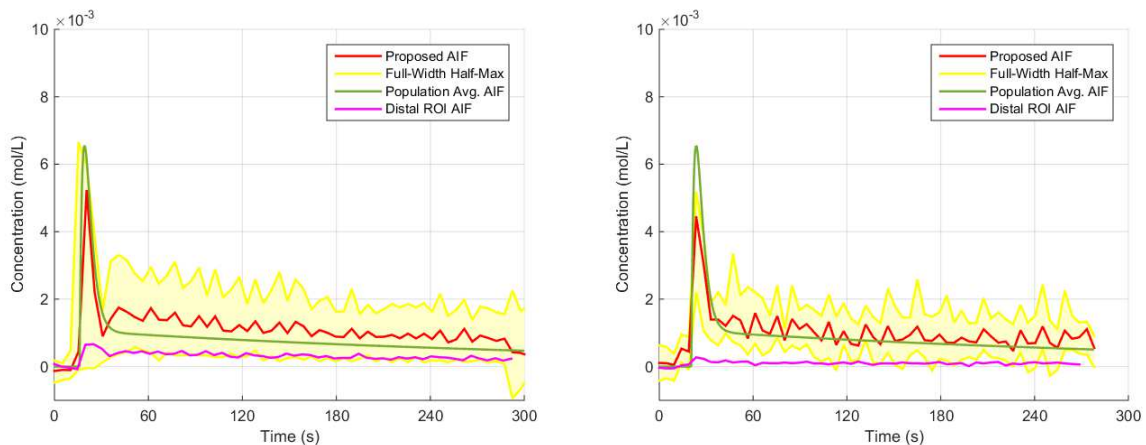


Figure 5.3a, b: AIFs of two subjects of the spine study, obtained with the proposed method (red), also showing the associated full-width at half-maximum intervals (yellow). AIFs obtained with the distal ROI method (magenta) and Orton's population-averaged AIF (green) are plotted for comparison.

The AIFs were used in the fitting of Tofts' model to the time-concentration curves in the bone marrow. The results of using the AIFs of the three methods as input is shown in Figure 5.4. No significant differences were found between the average RMSEs of the three AIF estimation methods ( $p > 0.05$ ). The distributions of the estimated PK parameters of all subjects in this dataset is shown as a boxplot in Figure 5.5. There was a significantly larger variance in the estimations of all four parameters by means of the distal ROI method, compared to the other methods ( $p < 0.05$  for all comparisons). Furthermore, the distal ROI approach yielded unrealistic estimations (e.g.,  $v_e > 1$ ) in several cases.

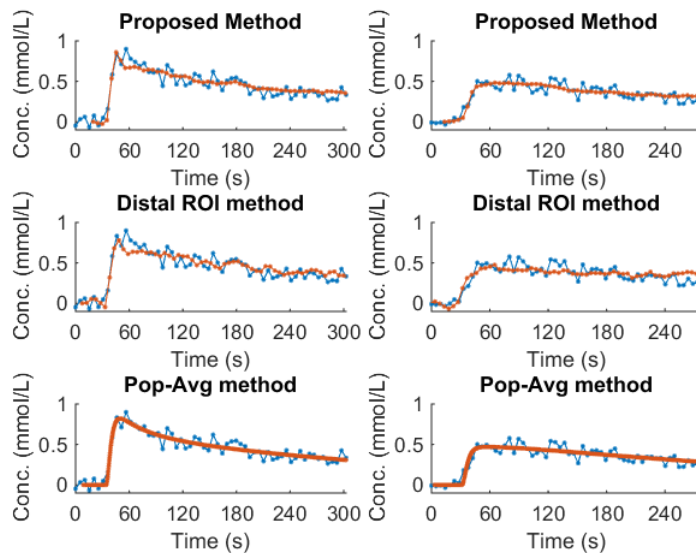


Figure 5.4: Fits of modelled time-concentration curves (red) to the measured time-concentration curves (blue) in vertebra of subjects of the spine study. Results of two subjects are shown columnwise. AIFs obtained with the proposed method (top row), distal ROI method (middle row) and population-average method (bottom row) were used as input to the PK model.

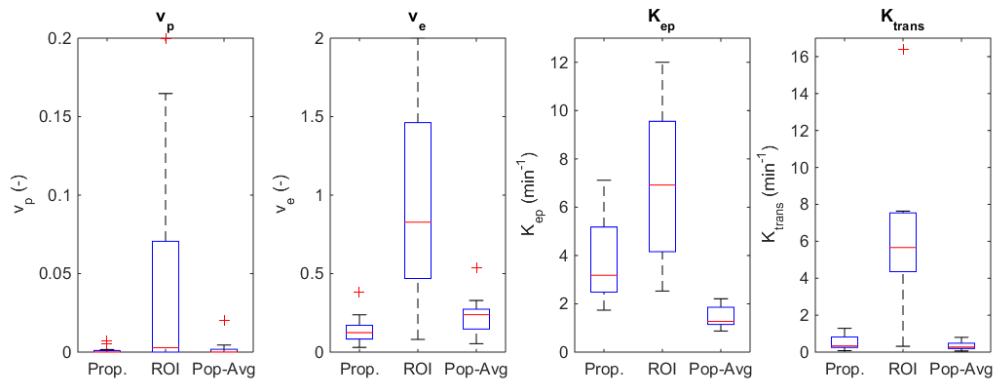


Figure 5.5: Boxplots showing the distributions of estimated PK parameters. The red lines represent the medians while the blue boxes reflect the 25<sup>th</sup> to 75<sup>th</sup> percentile ranges; whiskers extend to the most extreme value inside 1.5 times the interquartile range; values outside these ranges are indicated as individual points.

### 5.3.2 Results from the Crohn's Disease data

Maximum intensity projections in the coronal direction of the computed  $n$ -maps of two representative patients are shown in Figure 5.6.

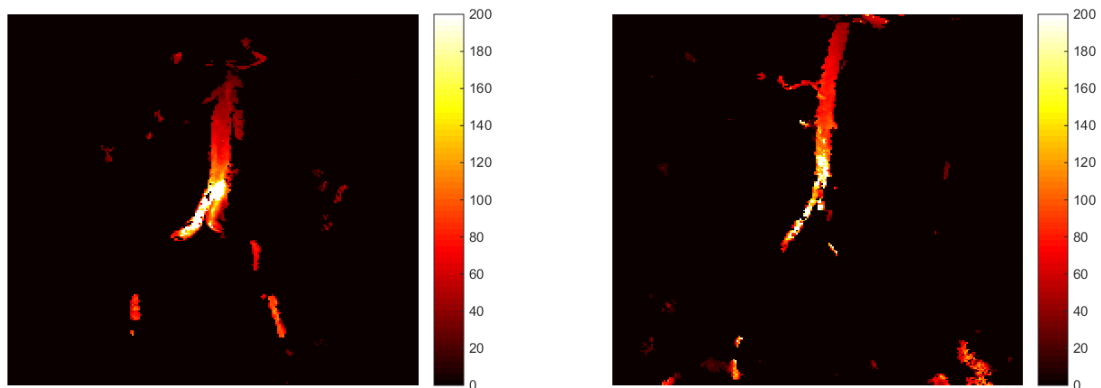


Figure 5.6: Crohn's patients study, coronal acquisition. Maximum intensity projections of  $n$ -maps of two representative datasets, showing the estimated number pulses in the segmented voxels. The segmentations were done automatically.

The modal AIFs corresponding to the  $n$ -maps of Figure 5.6 are shown in Figure 5.7. The AIFs estimated with the distal ROI method and the population-averaged AIF are also shown for comparison.

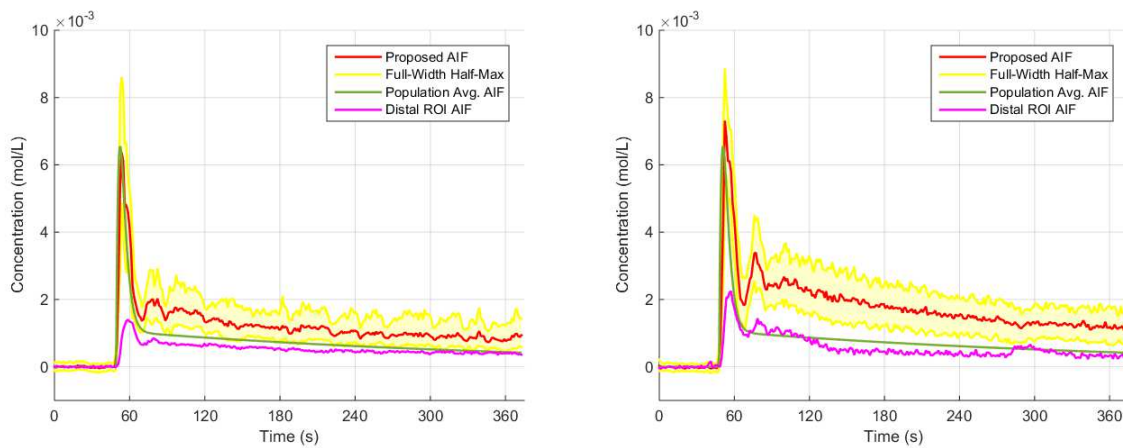


Figure 5.7: Two estimated AIFs determined for the same patients as in Figure 5.6. Red: Modal estimated AIF; Yellow: Full-width at half-maximum; Green: Orton's population-average AIF; Magenta: AIF estimated with the distal ROI method.

Fitting of Tofts' model to the time-concentration curves of bowel tissue in two subjects of the Crohn's Disease data, using AIFs obtained with each of the three methods, is shown in Figure 5.8. The difference in average RMSE between the three methods are not significant ( $p > 0.49$ ). The distributions of the estimated PK parameters of all subjects in this dataset is shown as a boxplot in Figure 5.9. There was a significantly higher median and larger variance in the estimations of  $v_p$  by means of the distal ROI method, compared to the other methods ( $p < 0.05$  in all comparisons).

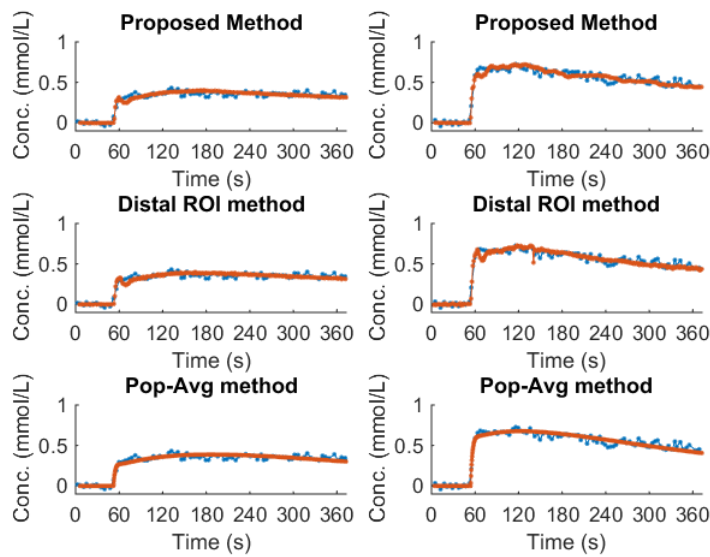


Figure 5.8: Tofts' model fitted to the measured time-concentration curves of two subjects of the Crohn's Disease study. Measured (blue) and modelled (red) time concentration curves in bowel tissue, using AIFs from the proposed (top), distal ROI (middle) and population-averaged (bottom) methods.

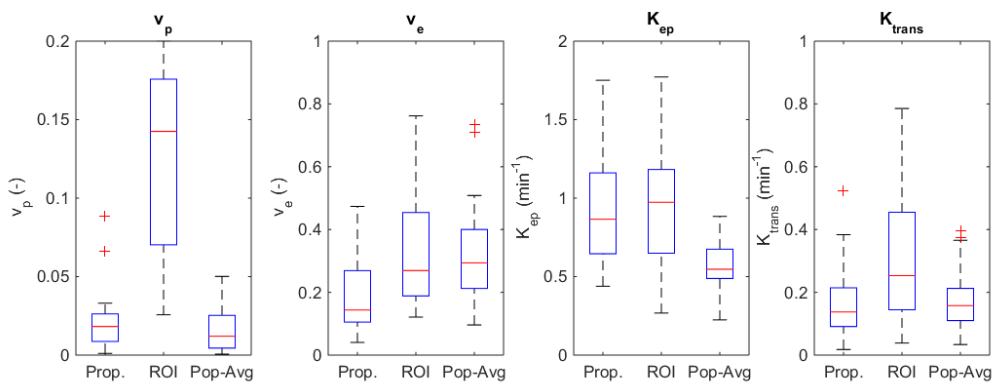


Figure 5.9: Boxplots showing the distributions of estimated PK parameters. The red lines represent the medians while the blue boxes reflect the 25<sup>th</sup> to 75<sup>th</sup> percentile ranges; whiskers extend to the most extreme value inside 1.5 times the interquartile range; values outside these ranges are indicated as individual points.

Further results of the PK analysis are shown in Figure 5.10. Here, the estimated  $K_{trans}$  parameters are plotted against the CDEIS scores, for each of the three methods. Linear fits are drawn with red lines. CDEIS scores were unavailable for two subjects, because the affected area could not be inspected by the gastroenterologist due to strictures in the bowel. Hence, the Spearman's rank



correlation coefficients were computed for  $N = 19$  subjects. A strong correlation of  $r = 0.733$  ( $p < 0.001$ ) was found when using the proposed method using an inflow-corrected AIF, while moderate correlations were found for the method using an AIF from a manually drawn ROI ( $r = 0.429$ ,  $p = 0.067$ ) and the population averaged AIF ( $r = 0.567$ ,  $p = 0.011$ ).

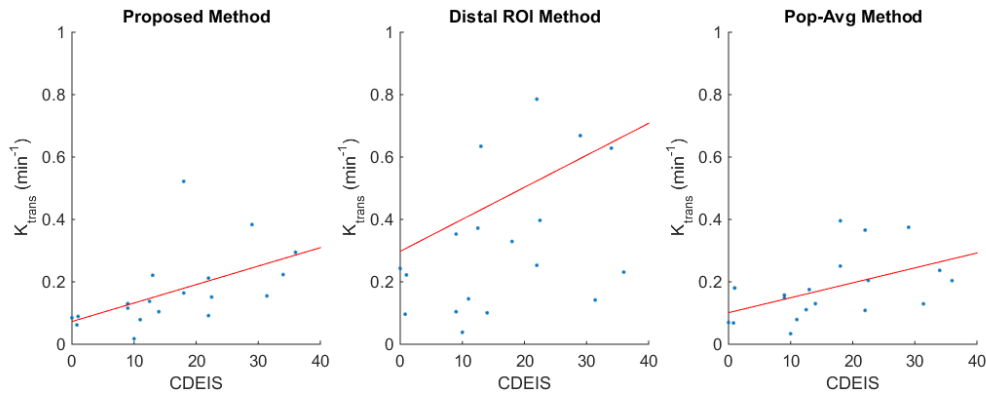


Figure 5.10: Result of the pharmacokinetic analyses of the second dataset.  $K_{trans}$  is plotted against the CDEIS score. Left: proposed method. Middle: ROI method. Right: population average method. The red lines are linear fits.

## 5.4 Discussion

### 5.4.1 The Spine Data

The results of the first patient study show that the proposed method can estimate AIFs from DCE-MRI scans with a variety of scan settings, even when inflow effects are severe. The reconstructed bolus peaks are clearly visible, and resemble those of the population-averaged AIF. This resemblance is expected, since the estimation of the number of pulses in each voxel relies on the area under the bolus peak, which is constrained to that of the population average.

The fit errors of Tofts' model using AIFs from the three methods are comparable. However, the AIF from the ROI method yields unrealistic PK model parameters despite the good fit. We did not observe significant differences between the medians and the associated variances in  $K_{trans}$  of the proposed method and the

population-average method. We did however observe differences in estimated model parameters in several cases. However, it is not possible to interpret this, for the lack of a reference standard.

#### **5.4.2 The Crohn's Disease Data**

An AIF could be estimated in each of the 21 subjects. Due to the increased temporal resolution (compared to the spine data), the second pass of the bolus was recognizable. As with the spine study data, the bolus peaks of the AIFs are in the same order of magnitude as that of the population-averaged model. The RMSE resulting from fitting Tofts' model is similar for each of the three methods. Again, the AIF from the ROI method yields unrealistic PK model parameters despite the good fit. We did not observe significant differences between the medians and the associated variances in  $K_{\text{trans}}$  of the proposed method and the population-average method.

For the 19 subjects for whom a CDEIS score was determined, a significant correlation of 0.733 ( $p < 0.001$ ) was found between the CDEIS score and the estimated  $K_{\text{trans}}$  parameter when using the proposed method. On the other hand, when using either of the other two AIF methods, lower correlations were found. This points to the fact that the estimation of  $K_{\text{trans}}$  using the AIF of the proposed method provides a better assessment of the severity of Crohn's Disease than when using the alternative methods.

#### **5.4.3 AIF Tail Offset**

In both patient studies, the concentration in the slowly decaying part of the AIFs (the "tails"), as estimated with the proposed method are slightly higher than those estimated with the other two methods. This is a result of the constraint imposed on the area under the bolus peak in the estimation of the number of pulses. This effect manifests in signal-ratio curves presenting a low bolus peak. Implicitly, this is assumed to be caused by the inflow effect, and accordingly, the estimated number of pulses will be low. This leads to a higher estimated concentration in both the peak and the tail.

The accuracy of our results is substantiated by considering the signal at two different time points of all segmented voxels in a subject from the Crohn's Disease dataset: the time point of maximum signal enhancement (i.e. at the bolus peak), and an arbitrary time point in the tail. See Figure 5.11. At both these time points, the concentration should be approximately the same in all segmented voxels. However, the signal ratio differs across these voxels, as a variable number of pulses is experienced by the spins. Figure 5.11 shows that the theoretical signal ratio for the estimated concentrations match the measured signal ratios in the artery, which means that the estimated concentration is accurate.

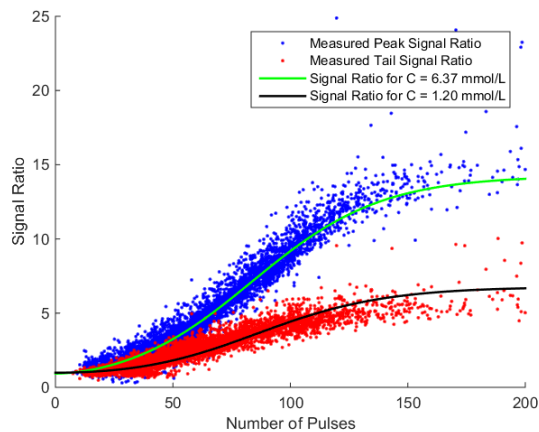


Figure 5.11: Signal ratio versus number of pulses. Blue and red dots: measured signal ratio in each segmented voxel at one time point during the bolus peak phase and tail phase respectively, plotted against the estimated number of pulses in that voxel. Green and black lines: theoretical signal ratios corresponding to the estimated concentration at said time points.

#### **5.4.4 Limitations**

A limitation of the proposed method is its dependence on the presence of a bolus peak. If the bolus peak is entirely not visible in the original DCE-MRI data, the number of pulses, and therefore the AIF, cannot be estimated reliably. In that case, it becomes impossible to precisely estimate the model parameters, such as the position of the bolus peak. This may occur, for example, when the temporal resolution is too low, and the bolus peak occurs between two time points.

Furthermore, the method relies on a proper segmentation of the artery. If the automated segmentation method wrongly includes regions outside the artery, the

estimated time-concentration curves at these locations may be unreliable. This is because the bolus peak becomes less well visible while a constant signal is mixed with the true AIF signal. A manual segmentation could be helpful in some cases, although this might not be desirable.

Some limitations of our experiment in the Crohn's Disease data relate to the limited number of patients and the annotation by merely one radiologist. As such, the outcome should be considered an indication of the improved reliability of our method compared to the conventional approaches.

Finally, the most important limitation is the lack of a reference standard. Obtaining a true time-concentration curve of contrast agent in flowing blood under realistic measurement circumstances is a highly complex, still unsolved issue.

## **5.5 Conclusion**

We applied a new subject-specific AIF estimation method to two patient cohorts, in order to study the merit of correcting for flow enhancement. With the spine dataset, we demonstrated that our approach resulted in realistic PK model parameters, while applying a range of scan settings. Using the Crohn's Disease dataset, we showed that our method facilitates significant correlation of  $K_{\text{trans}}$  with CDEIS. What is more, our subject specific approach yielded significantly higher correlation than a method relying on a population-average AIF. Other applications of pharmacokinetic modelling may also benefit from our method, since it is generally applicable.

## **5.6 Acknowledgements**

The research presented in this paper was funded from the European Union's Seventh Framework Programme (FP7/2007-2013): the VIGOR++ Project (grant agreement nr. 270379).

## 5.7 Appendix

### 5.7.1 Aorta segmentation from the Crohn's Disease data

The aorta was segmented from the background based on two properties: the time-to-peak is the shortest of all tissue voxels, and the voxels react to the injection of contrast agent. This was accomplished by sorting all TICs of a dataset by the time point at which the maximum signal occurred (the time-to-peak). Subsequently, all TICs with the same time-to-peak were averaged, and each such average TIC was converted to a signal-ratio curve by dividing by its intensity at the first time point. An example is shown in Figure 5.12. Here, the transition from left to right indicates the arrival of contrast agent, while the transition from top to bottom shows whether or not voxels enhance due to contrast agent. The area near the top mainly consists of non-tissue voxels, which happen to have their maximum signal ratio before the arrival of contrast agent, due to noise. The minimum valid time to peak and the average time of contrast onset were determined by fitting the product of two error functions to Figure 5.12, and only the voxels within a small range (2 time points) around the minimum valid time to peak were retained. Next, the relative contrast enhancement (RCE) of the remaining voxels was computed individually, using the computed minimum time to peak as boundary between pre-contrast and post-contrast. Discarding any voxels with  $RCE < 1$  served to remove more unreliable voxels. Finally, voxels that were not part of a larger cluster of voxels were assumed to be noise, and were discarded. The remaining voxels were then assumed to compose the aorta.

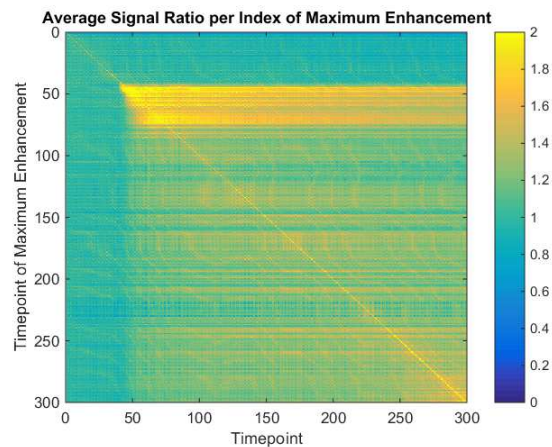


Figure 5.12: Signal-ratio curves sorted by the time to peak, and averaged. The arrival of contrast agent is seen from left to right, while the top-bottom transition shows whether or not a voxel reacts to contrast agent.

## 5.8 References

1. Hemke R, Lavini C, Nusman CM, van den Berg JM, Dolman KM, Schonenberg-Meinema D, van Rossum MA, Kuijpers TW, Maas M. Pixel-by-pixel analysis of DCE-MRI curve shape patterns in knees of active and inactive juvenile idiopathic arthritis patients. *European radiology* 2014;24(7):1686-1693.
2. Chen WT, Shih TT, Chen RC, Lo SY, Chou CT, Lee JM, Tu HY. Vertebral bone marrow perfusion evaluated with dynamic contrast-enhanced MR imaging: significance of aging and sex. *Radiology* 2001;220(1):213-218.
3. Zollner FG, Zimmer F, Klotz S, Hoeger S, Schad LR. Renal perfusion in acute kidney injury with DCE-MRI: deconvolution analysis versus two-compartment filtration model. *Magnetic resonance imaging* 2014;32(6):781-785.
4. Lim SW, Chrysochou C, Buckley DL, Kalra PA, Sourbron SP. Prediction and assessment of responses to renal artery revascularization with dynamic contrast-enhanced magnetic resonance imaging: a pilot study. *American journal of physiology Renal physiology* 2013;305(5):F672-678.
5. Tofts PS, Brix G, Buckley DL, Evelhoch JL, Henderson E, Knopp MV, Larsson HB, Lee TY, Mayr NA, Parker GJ, Port RE, Taylor J, Weisskoff RM. Estimating kinetic parameters from dynamic contrast-enhanced T(1)-

- weighted MRI of a diffusible tracer: standardized quantities and symbols. *Journal of magnetic resonance imaging* : JMRI 1999;10(3):223-232.
6. Parker GJ, Roberts C, Macdonald A, Buonaccorsi GA, Cheung S, Buckley DL, Jackson A, Watson Y, Davies K, Jayson GC. Experimentally-derived functional form for a population-averaged high-temporal-resolution arterial input function for dynamic contrast-enhanced MRI. *Magnetic resonance in medicine* 2006;56(5):993-1000.
  7. Jensen RL, Mumert ML, Gillespie DL, Kinney AY, Schabel MC, Salzman KL. Preoperative dynamic contrast-enhanced MRI correlates with molecular markers of hypoxia and vascularity in specific areas of intratumoral microenvironment and is predictive of patient outcome. *Neuro Oncol* 2014;16(2):280-291.
  8. Taouli B, Johnson RS, Hajdu CH, Oei MT, Merad M, Yee H, Rusinek H. Hepatocellular carcinoma: perfusion quantification with dynamic contrast-enhanced MRI. *AJR Am J Roentgenol* 2013;201(4):795-800.
  9. Rijpkema M, Kaanders JH, Joosten FB, van der Kogel AJ, Heerschap A. Method for quantitative mapping of dynamic MRI contrast agent uptake in human tumors. *J Magn Reson Imaging* 2001;14(4):457-463.
  10. Aronhime S, Calcagno C, Jajamovich GH, Dyvorne HA, Robson P, Dieterich D, Fiel MI, Martel-Laferriere V, Chatterji M, Rusinek H, Taouli B. DCE-MRI of the liver: effect of linear and nonlinear conversions on hepatic perfusion quantification and reproducibility. *J Magn Reson Imaging* 2014;40(1):90-98.
  11. Fram EK, Herfkens RJ, Johnson GA, Glover GH, Karis JP, Shimakawa A, Perkins TG, Pelc NJ. Rapid calculation of T1 using variable flip angle gradient refocused imaging. *Magnetic resonance imaging* 1987;5(3):201-208.
  12. Stalder AF, von Elverfeldt D, Paul D, Hennig J, Markl M. Variable echo time imaging: Signal characteristics of 1-M gadobutrol contrast agent at 1.5 and 3T. *Magnetic Resonance in Medicine* 2008;59(1):113-123.
  13. Garpebring A, Wirestam R, Ostlund N, Karlsson M. Effects of inflow and radiofrequency spoiling on the arterial input function in dynamic contrast-enhanced MRI: a combined phantom and simulation study. *Magnetic resonance in medicine* 2011;65(6):1670-1679.
  14. Orton MR, d'Arcy JA, Walker-Samuel S, Hawkes DJ, Atkinson D, Collins DJ, Leach MO. Computationally efficient vascular input function models

- for quantitative kinetic modelling using DCE-MRI. *Physics in Medicine and Biology* 2008;53(5):1225-1239.
15. Ivancevic MK, Zimine I, Montet X, Hyacinthe JN, Lazeyras F, Foxall D, Vallee JP. Inflow effect correction in fast gradient-echo perfusion imaging. *Magnetic resonance in medicine* 2003;50(5):885-891.
  16. de Simone G, Devereux RB, Daniels SR, Mureddu G, Roman MJ, Kimball TR, Greco R, Witt S, Contaldo F. Stroke volume and cardiac output in normotensive children and adults. Assessment of relations with body size and impact of overweight. *Circulation* 1997;95(7):1837-1843.
  17. Cheng YZ. Mean Shift, Mode Seeking, and Clustering. *Ieee T Pattern Anal* 1995;17(8):790-799.
  18. de Bazelaire CM, Duhamel GD, Rofsky NM, Alsop DC. MR imaging relaxation times of abdominal and pelvic tissues measured in vivo at 3.0 T: preliminary results. *Radiology* 2004;230(3):652-659.
  19. Li Z, Tielbeek JA, Caan MW, Puylaert CA, Ziech ML, Nio CY, Stoker J, van Vliet LJ, Vos FM. Expiration-phase template-based motion correction of free-breathing abdominal dynamic contrast enhanced MRI. *IEEE transactions on bio-medical engineering* 2015;62(4):1215-1225.





# 6 Conclusion

---

This thesis presents two important methods to improve quantitative pharmacokinetic analysis of Dynamic Contrast Enhanced MRI. We have introduced a new method for accurately estimating the  $T_1$ -value of tissues in the presence of  $B_1$ -inhomogeneities. We then created a novel method for estimating the concentration of contrast agent in flowing blood, i.e., the arterial input function (AIF). In this chapter, we highlight the conclusions of the presented work, and recommend future work.

## 6.1 Simultaneous $T_1$ - and $B_1$ -mapping

In the third chapter, we studied the feasibility of a method to simultaneously obtain a pre-contrast  $T_1$ -map, as well as a  $B_1$ -inhomogeneity map. This proved to be challenging, particularly due to the low signal-to-noise ratio arising from imaging within tight time constraints. We used two different MRI scans, namely a Look-Locker (LL) scan and a Variable Flip Angle (VFA) scan, both of which could be obtained within breath holds. Both scans can be used separately to compute a  $T_1$ -map, but the LL method yields a noisy, low-resolution  $T_1$ -map (especially on 1.5T), while the VFA method is very susceptible to  $B_1$ -inhomogeneities.

We combined the information of the two scans, in order to produce a  $T_1$ -map of comparable quality as a  $T_1$ -map obtained using the conventional VFA method, while correcting for possible attenuation of the  $B_1$ -field. Furthermore, we estimated the  $B_1$ -attenuation itself, which can be used to correct the flip angle of other scans (e.g., the FSPGR sequence used in DCE-MRI).

We found that a reliable  $T_1$ -map could be computed, which was validated using both a phantom study and a study on human volunteers. The phantom study showed that the procedure yields a substantially smaller mean deviation in  $T_1$  from the reference standard (Inversion Recovery) than an uncorrected VFA approach. The volunteer study showed both a more accurate estimation of  $T_1$  and a reduced influence of the  $B_1$ -inhomogeneity on the signal intensity.

In short, the proposed method combines the high resolution of the VFA method with the  $B_1$  stability of the LL method.

## 6.2 Estimating the AIF with Compensation for Flow Enhancement

In Chapters 4 and 5, we presented a new method to estimate the AIF from DCE-MRI data that compensates for the inflow effect, and tested the method on two patient datasets. The inflow effect is present when new spins flow into the field of view during acquisition, and complicates a reliable estimation of the contrast agent concentration. Our method takes the spin dynamics during the transient state of an FSPGR sequence into account, including the  $T_2^*$  decay.

In order to estimate the AIF, the proposed method resolves the ambiguity between signal enhancement due to the presence of contrast agent and signal enhancement due to the inflow effect. Specifically, the number of RF-pulses that spins have received is estimated first, using a population averaged AIF as prior information. Then, the flow enhancement is compensated as the signal intensity is converted into concentration.

In the theoretical part (Chapter 4), we found that the proposed method accurately corrects for the inflow effects on computer generated AIFs. The simulations showed that the proposed method sustains accurate estimation of the number of pulses that flowing spins received, and that the concentration of contrast agent could be quantified accurately. Furthermore, we found that the method could correctly estimate the flow velocity in a controlled flow phantom experiment, which confirms that the proposed method is in agreement with the theory.

In the application part (Chapter 5), we found that the proposed AIF estimation method is applicable to DCE-MRI data acquired with varying scan settings. We found that the compensation for the inflow effect is indeed necessary: the AIF was severely underestimated when estimating the AIF in a distal region of interest that is assumed to not suffer from inflow effects. Also, using data from Crohn's Disease patients, we found that the  $K_{trans}$  parameter of Tofts' pharmacokinetic model correlated better with the clinically relevant CDEIS score when using the AIF from the proposed method, compared to the alternatives.

### 6.3 Future Work

The following topics may be expanded upon in the future.

*Methodology* – The current method for estimating the AIF relies on the magnitude of the MRI signal. It is well known that the phase component also contains information about the concentration. The AIF might be further improved by integrating phase information in the estimation of the contrast agent concentration.

*Refinement* – A challenging issue, which we did not study, is the estimation of the  $T_1$  value of blood. In our work (Chapter 5), we adopted a value from the literature in order to perform pharmacokinetic analyses. The  $T_1$  value might be estimated using the methodology of Chapter 3, while taking into account the flow effects estimated by an independent method.

*Validation* – In medical image analysis, it is often difficult or impossible to obtain a gold standard with which to compare results. Still, it is important that new methods are accurate. In the case of estimating an AIF from flowing blood, a ground truth is hard to establish, but some insight might be obtained by means of other imaging modalities, such as CT or PET (with different contrast agents). Also, the estimation of PK parameters would benefit from validation using a gold standard.

*Application* – The methods presented in this thesis are applied to a limited number of cases: healthy volunteers for the  $T_1$ -mapping, and patients with spine related injuries or Crohn's Disease for the AIF estimation. Clearly, the methods can be used in many other applications, to improve the measurement of physical or physiological properties of tissues.

*Integration* – Pharmacokinetic analysis using DCE-MRI is only a link in a longer chain of assessing pathology. The complete pipeline includes automatic registration of MRI images, measuring image features (pharmacokinetic or otherwise), and consolidating these measurements into beneficial information for medical doctors. The VIGOR++ project initiated a framework for this process, for the assessment of Crohn's Disease severity, and the methods presented in this thesis could be integrated readily.

# Summary

---

Dynamic Contrast Enhanced MRI is an important technique to assess the pharmacokinetic properties of tissues. This thesis addresses two major steps necessary for quantitative DCE-MRI: the estimation of the tissue's  $T_1$ -time and local  $B_1$ -field strength, and the estimation of the time-dependent concentration of contrast agent in the blood supply to the tissue of interest.

In quantitative pharmacokinetic analysis, the perfusion and vascularization of tissues are estimated by measuring the response to an intravenous injection of contrast agent. This analysis relies on knowledge of the concentrations of contrast agent in both the tissue and in the blood perfusing the tissue. The contrast agent affects the  $T_1$  relaxation time of the tissue, and if the  $T_1$ -time of a tissue is known, the concentration profile can be computed. However, local  $B_1$ -inhomogeneities can affect the MRI signal strength, complicating the measurement of  $T_1$  using conventional methods. Furthermore, the inflow of fresh blood into the field of view causes an additional, location dependent signal enhancement in the blood, which makes a direct measurement of the  $T_1$ -time (and thus the concentration) in blood impossible.

This thesis introduces a new method to estimate a  $T_1$ -map of tissues in the presence of  $B_1$ -inhomogeneities. We do this by combining two MRI scans that can each be acquired within breath-holds: one that yields a precise  $T_1$ -map, though biased by the inhomogeneous  $B_1$ -field; and one that delivers an unbiased, but imprecise estimate. Combining the information of these two scans yields an estimate of the  $B_1$ -field, which is then used to correct the  $T_1$ -map. We validate our method in a phantom study, and in an *in vivo* study. We found that the proposed method successfully merges the high resolution of the first method with the insensitivity to  $B_1$ -inhomogeneities of the second.

This thesis also introduces a new method to estimate the time-dependent concentration of contrast agent in blood (i.e., the arterial input function (AIF)),

which is affected by signal enhancement due to the inflow effect. We do this by first estimating the number of RF-pulses by incorporating knowledge about the average AIF in a population. We then use the number of pulses to re-estimate the concentration from the measured MRI signal, thereby correcting for the inflow effect. We validate our method by means of Monte Carlo simulations and with a controlled flow phantom experiment. We then apply our method to two patient datasets, and use the estimated arterial input function for pharmacokinetic modelling. The first dataset consisted of patients with spine related injuries, and was acquired under a variety of scan settings to assess the method's robustness. The second dataset consisted of patients with Crohn's Disease which had a clinically relevant CDEIS score available. In both datasets, we found that our method yields realistic pharmacokinetic model parameters. Instead, estimating the AIF from a distally placed region of interest, as is often done in literature, led to large variation and unrealistic parameters. Furthermore, in the Crohn's patients we found a better correlation between the estimated pharmacokinetic parameter  $K_{\text{trans}}$  and the CDEIS score, compared to traditional methods.

Though the rationale for developing these methods were the presence of  $B_1$ -inhomogeneities, and pronounced inflow effects in the aorta, other applications of pharmacokinetic modelling (e.g., in other parts of the body) may benefit from our methods, since they are generally applicable.

Jeroen J.N. van Schie

# Samenvatting

---

Dynamisch Contrastversterkt MRI is een belangrijke techniek om de farmacokinetische eigenschappen van weefsels te bepalen. Dit proefschrift richt zich op twee belangrijke onderdelen voor kwantitatieve DCE-MRI: het schatten van de  $T_1$ -tijd en lokale  $B_1$ -veldsterkte van een weefsel, en het schatten van de tijdafhankelijke concentratie van contrastmiddel in de bloedtoevoer van het weefsel.

Bij kwantitatieve farmacokinetische analyse worden de perfusie en vascularisatie van weefsels geschat door de reactie van dat weefsel op een intraveneuze injectie van contrastmiddel te meten. De analyse vereist dat de concentratie van het contrastmiddel bekend is in zowel het weefsel als in de bloedtoevoer. Het contrastmiddel beïnvloedt de  $T_1$  relaxatietijd van het weefsel, en het concentratieprofiel kan worden berekend als de  $T_1$ -tijd bekend is. Echter, lokale  $B_1$ -inhomogeniteiten kunnen het MRI signaal beïnvloeden, wat het schatten van de  $T_1$ -tijd met conventionele methoden bemoeilijkt. Daarnaast veroorzaakt de instroom van nieuw bloed in het field of view een extra, locatieafhankelijke versterking van het MRI signaal, wat een directe meting van de  $T_1$ -tijd (en dus de concentratie) in bloed onmogelijk maakt.

Dit proefschrift introduceert een nieuwe methode om de  $T_1$ -tijd van weefsels in kaart te brengen, ondanks de aanwezigheid van  $B_1$ -inhomogeniteiten. We doen dit door twee verschillende MRI scans, die elk binnen periodes van ademstilstand kunnen worden verkregen, te combineren. De ene scan geeft een precieze  $T_1$ -kaart, maar wordt sterk beïnvloed door het inhomogene  $B_1$ -veld; de andere scan geeft wel een zuivere schatting, maar is niet erg precies. Door deze twee scans te combineren, wordt de sterkte van het  $B_1$ -veld geschat, wat vervolgens wordt gebruikt om de  $T_1$ -kaart te corrigeren. We hebben deze methode gevalideerd met behulp van een fantoom, en met een *in vivo* studie. We bevonden dat de door ons voorgestelde methode de hoge resolutie van de eerste methode goed kon samenvoegen met de ongevoeligheid voor  $B_1$ -inhomogeniteiten van de tweede methode.



Dit proefschrift introduceert ook een nieuwe methode om de tijdsafhankelijke concentratie van contrastmiddel in bloed (de arteriële input functie (AIF)) te schatten, waarvan het MRI signaal werd beïnvloed door het instroomeffect. We doen dit door eerst het aantal RF-pulsen te schatten, door kennis van de gemiddelde AIF in een populatie als referentie te gebruiken. Daarna gebruiken we het berekende aantal pulsen om de concentratie te schatten uit het MRI signaal, waarmee we dus corrigeren voor het instroomeffect. We hebben onze methode gevalideerd met Monte Carlo simulaties, en met een fantoomexperiment. Daarna hebben we onze methode toegepast op data van twee groepen patiënten, waarna we de geschatte arteriële input functies hebben gebruikt voor farmacokinetische analyses. De data van de eerste groep kwam van patiënten met klachten gerelateerd aan de wervelkolom, en was gescand met een reeks van verschillende instellingen om de robuustheid van de methode te testen. De tweede groep data kwam van patiënten met de ziekte van Crohn, en waarvan ook een klinisch relevante CDEIS score beschikbaar was. In beide groepen bevonden we dat onze methode realistische farmacokinetische parameters opleverde. Omgekeerd, de AIF schatten uit een distaal geplaatst gebied, zoals vaak in de literatuur wordt gedaan, levert een grote spreiding en onrealistische parameters op. Verder, bij de patiënten met de ziekte van Crohn bevonden we een betere correlatie tussen de farmacokinetische parameter  $K_{\text{trans}}$  en de CDEIS score, vergeleken met de traditionele methoden.

De motivering voor het ontwikkelen van deze methoden kwam oorspronkelijk uit de aanwezigheid van  $B_1$ -inhomogeniteiten, en van sterke instroomeffecten in de aorta. Echter, andere farmacokinetische toepassingen kunnen ook gebruikmaken van onze methoden (bijvoorbeeld in andere delen van het lichaam), aangezien ze algemeen toepasbaar zijn.

Jeroen J.N. van Schie

# Acknowledgements

---

This is the end of my thesis, where I express my gratitude towards those who helped me produce this work. Without your contributions, I would not be able to complete this thesis.

First of all, I would like to thank my supervisors: Frans, Lucas, Cristina and Jaap. Thanks to your welcome advice, our insightful discussions, and countless iterations of revisions, this thesis became what it is now. Over the course of the project, you helped me gain an understanding of the intricacies of MRI, both from a physics point of view and from a medical point of view.

Secondly, the research presented in this thesis would not have been possible without the anonymous volunteers who underwent the arduous MRI protocols, to provide the necessary data. I thank the patients from the VIGOR++ study, and the patients from the spine study, and also the healthy volunteers.

Furthermore, I would like to thank the colleagues whom I worked with over the course of my project. My officemates, Jelena and Tian. My research colleagues and travel companions, Robiël and Zhang. All the other people of the Quantitative Imaging group: Alex, Anna, Annelies, Babak, Jelle, Jeroen, Jianfei, Joor, Juan Pedro, Kadir, Lena, Lennard, Mandy, Miloš, Mojtaba, Nadya, Qiaole, Robert, Ron, Ronald, Tom, and all the others. Thank you for the great time together during the coffee and lunch breaks, during our teaching assistances, and during the awesome seasonal events.

I am also grateful for the contributions of people from the AMC: Aart, Bram, Carl, Erik, Jeroen, Jurgen and Wouter, and the people from the VIGOR++ project: Alexander, Ernst, Jesica, Laurence, Rado and the others.

Finally, I thank my friends and family for the support and for being there, and for providing the balance between work and life. Dank jullie wel!

# Curriculum Vitae

---

Jeroen Johannes Nicolaas van Schie was born on 5 May 1986 in Naaldwijk, the Netherlands. He obtained his high school diploma in 2005 at the Interconfessionele Scholengemeenschap het Westland in 's-Gravenzande. He subsequently enrolled at the Technische Universiteit Delft (Delft University of Technology), where he received his Bachelor degree in Applied Physics (Technische Natuurkunde) in 2008, and his Master degree in Applied Physics in 2011. After an internship with Philips Medical in Best, the Netherlands, he returned to the Quantitative Imaging group in Delft to work on his PhD project. During his PhD project, he was involved in the international VIGOR++ project.